

**Localized states in the conserved Swift-Hohenberg equation with cubic nonlinearity**Uwe Thiele,<sup>\*</sup> Andrew J. Archer, and Mark J. Robbins*Department of Mathematical Sciences, Loughborough University, Loughborough, Leicestershire LE11 3TU, United Kingdom*

Hector Gomez

*University of A Coruna, Campus de Elvina, 15192 A Coruna, Spain*

Edgar Knobloch

*Department of Physics, University of California, Berkeley, California 94720, USA*

(Received 21 January 2013; revised manuscript received 21 March 2013; published 15 April 2013)

The conserved Swift-Hohenberg equation with cubic nonlinearity provides the simplest microscopic description of the thermodynamic transition from a fluid state to a crystalline state. The resulting phase field crystal model describes a variety of spatially localized structures, in addition to different spatially extended periodic structures. The location of these structures in the temperature versus mean order parameter plane is determined using a combination of numerical continuation in one dimension and direct numerical simulation in two and three dimensions. Localized states are found in the region of thermodynamic coexistence between the homogeneous and structured phases, and may lie outside of the binodal for these states. The results are related to the phenomenon of slanted snaking but take the form of standard homoclinic snaking when the mean order parameter is plotted as a function of the chemical potential, and are expected to carry over to related models with a conserved order parameter.

DOI: [10.1103/PhysRevE.87.042915](https://doi.org/10.1103/PhysRevE.87.042915)

PACS number(s): 05.45.-a, 05.70.-a, 64.70.D-

**I. INTRODUCTION**

Spatially localized structures (LS) are observed in a great variety of pattern-forming systems. Such states include spotlike structures found in reaction-diffusion systems [1] and in a liquid light-valve experiment [2], isolated spikes observed in a ferrofluid experiment [3], and localized buckled states resulting from the buckling of slender structures under compression [4]. Related states are observed in fluid mechanics, including convection [5–7] and shear flows [8]. In other systems, such as Faraday waves, the LS oscillate in time, either periodically or with a more complex time dependence, forming structures referred to as oscillons [9,10]. This is also the case for oscillons in granular media [11] and in optics [12]. Other examples of LS include localized traveling waves [13,14] and states called “worms” observed in electroconvection [15,16]. In many of these systems, the use of envelope equations removes the (fast) time dependence and maps such time-dependent structures onto equilibria.

Many of the structures mentioned above are examples of “dissipative solitons” [17] in which energy loss through dissipation is balanced by energy input through spatially homogeneous forcing. Others (e.g., [3,4]) correspond to local minima of an underlying energy or Lyapunov functional. This is the case for systems whose dynamics are of gradient type, provided only that the energy is bounded from below. On finite domains with null boundary conditions, such systems evolve to steady states which may or may not correspond to LS. However, in generic systems supporting dissipative solitons no Lyapunov function will be present and the evolution of the system may be nonmonotonic.

In either system type, time-independent LS are found in regions of parameter space in which a time-independent spatially homogeneous (i.e., uniform) state coexists with a time-independent spatially periodic state. Within this region there is a subregion referred to as the *snaking* or *pinning* region [18] in which a great variety of stationary LS are present. In the simplest, one-dimensional, case the LS consist of a segment of the periodic state embedded in a homogeneous background; segments of the homogeneous state embedded in periodic background may be thought of as localized hole states (LH). Steady states of this type lie on a pair of intertwined branches that snake back and forth across the snaking region, one of which consists of reflection-symmetric LS with a peak in the center, while the other consists of similar states but with a dip in the center, and likewise for the holes. Near the left edge of the snaking region, each LS adds a pair of new peaks, one at either end, and these grow to full size as one follows the LS across the snaking region to its right edge, where both branches turn around and the process repeats. Thus, as one follows the LS branches toward larger  $L^2$  norm, both types of LS gradually grow in length, and all such structures coexist within the snaking region. On a finite interval the long LS take the form of holes in an otherwise spatially periodic state, but on the real line, the LS and LH remain distinct although both occupy the same snaking region. The LS branches are, in addition, interconnected by cross-links resembling the rungs of a ladder, consisting of asymmetric LS [19]. In generic systems posed on the real line, states of this type drift, either to the left or the right, depending on the asymmetry, but in systems with gradient dynamics the asymmetric states are also time-independent. These, along with bound states of two, three, etc. LS/LH, are also present within the snaking region [19].

The above behavior is typical of nonconserved order parameter fields. However, an important subclass of gradient

---

<sup>\*</sup>u.thiele@lboro.ac.uk

systems possesses a conserved quantity, and in such systems the order parameter field has a fixed mean value. Systems of this type arise frequently in fluid convection and other applications [20–22] and are distinguished from the standard scenario summarized above by the following properties [23,24]: (i) the snaking becomes slanted (sometimes referred to as “sidewinding”), (ii) LS may be present outside of the region of coexistence of the homogeneous and periodic states, (iii) LS are present even when the periodic states bifurcate supercritically, i.e., when the coexistence region is absent entirely. The slanting of the snakes-and-ladders structure is a finite-size effect: in a finite domain, expulsion of the conserved quantity from the LS implies its overabundance outside (or vice versa), a fact that progressively delays (to stronger forcing) the formation events whereby the LS grow in length. The net effect is that LS are found in a much broader region of parameter space than in nonconserved systems.

The above properties are shared by many of the models arising in dynamical density functional theory (DDFT) and related phase field models of crystalline solids. The simplest such phase field crystal (PFC) model [25] (see below) leads to the so-called conserved Swift-Hohenberg (cSH) equation. This equation was first derived, to the authors’ knowledge, as the equation governing the evolution of binary fluid convection between thermally insulating boundaries [26]; for recent derivations in the PFC context, see Refs. [25,27,28]. In this connection, the PFC model may be viewed as probably the simplest *microscopic* model for the freezing transition that can be constructed. In this model, the transition from a homogeneous state to a periodic state corresponds to the transition from a uniform density liquid to a periodic crystalline solid. The LS of interest in this model then correspond to states in which a finite-size portion of the periodic crystalline phase coexists with the uniform density liquid phase, and these are expected to be present in the coexistence region between the two phases. Some rather striking examples of LS in large two-dimensional systems include snowflake-like and dendritic structures, e.g., Refs. [25,29–32]. In fact, as shown below, the LS are also present at state points outside of the coexistence region, at least in one spatial dimension. However, despite the application of the cSH (or PFC) equation in this and other areas, the detailed properties of the LS described by this equation have not been investigated. In this paper, we make a detailed study of the properties of this equation in one spatial dimension with the aim of setting this equation firmly in the body of literature dealing with spatially localized structures. Our results are therefore interpreted within both languages, in an attempt to make the existing understanding of LS accessible to those working on nonequilibrium models of solids, and to use the simplest PFC model to exemplify the theory. In addition, motivated by Refs. [29–32], we also describe related results in two and three dimensions, where (many) more types of regular patterns are present and hence many more types of LS. Our work focuses on “bump” states (also referred to as “spots”) which are readily found in direct numerical simulations of the conserved Swift-Hohenberg equation as well as in other systems [2].

Although the theory for these cases in two and three dimensions is less well developed [33,34], continuation results indicate that some of the various different types of LS can

have quite different properties. For example, the bump states differ from the target-like LS formed from the stripe state that can also be seen in the model. In particular, spots in the nonconserved Swift-Hohenberg equation in the plane bifurcate from the homogeneous state regardless of whether stripes are subcritical or supercritical [35]; see also Ref. [36]. The key question, hitherto unanswered, is whether two-dimensional structures in the plane snake indefinitely and likewise for three-dimensional structures.

The paper is organized as follows. In Sec. II, we describe the conserved Swift-Hohenberg equation and its basic properties. In Sec. III, we describe the properties of LS in one spatial dimension as determined by numerical continuation. In Sec. IV, we describe related results in two and three spatial dimensions, but obtained by direct numerical simulation of the PFC model. Since this model has a gradient structure, on a finite domain all solutions necessarily approach a time-independent equilibrium. However, as we shall see, the number of competing equilibria may be very large and different equilibria are reached depending on the initial conditions employed. In Sec. V, we put our results into context and present brief conclusions.

## II. THE CONSERVED SWIFT-HOHENBERG EQUATION

### A. Equation and its variants

We write the cSH (or PFC) equation in the form

$$\partial_t \phi(\mathbf{x}, t) = \alpha \nabla^2 \frac{\delta F[\phi]}{\delta \phi(\mathbf{x}, t)}, \quad (1)$$

where  $\phi(\mathbf{x}, t)$  is an order parameter field that corresponds in the PFC context to a scaled density profile,  $\alpha$  is a (constant) mobility coefficient, and  $F[\phi]$  denotes the free-energy functional,

$$F[\phi] \equiv \int d\mathbf{x} \left[ \frac{\phi}{2} [r + (q^2 + \nabla^2)^2] \phi + \frac{\phi^4}{4} \right]. \quad (2)$$

Here  $\mathbf{x} = (x, y, z)$ ,  $\nabla = (\partial_x, \partial_y, \partial_z)^T$  is the gradient operator, and subscripts denote partial derivatives. It follows that the system evolves according to the cSH equation,

$$\partial_t \phi = \alpha \nabla^2 [r\phi + (\nabla^2 + q^2)^2 \phi + \phi^3]. \quad (3)$$

Equation (3) is sometimes called the derivative Swift-Hohenberg equation [37,38]. We prefer the terminology “conserved” to indicate that it is an equation for a conserved order parameter; the terminology “conservative” is precluded by the dissipative nature of its dynamics. Many papers use a different sign convention for the parameter  $r$  (e.g., [27,29,39–45]). In this equation, the quartic term in  $F[\phi]$  may be replaced by other types of nonlinearity, such as  $f_{23} = -b_2 \phi^3/3 + \phi^4/4$  [27,29,37,38] without a substantial change in behavior. Related but nonconserved equations  $\partial_t \phi = -\tilde{\alpha} \delta F[\phi]/\delta \phi$  with nonlinear terms of the form  $f_{23}$  [46] or  $f_{35} = -b_3 \phi^4/4 + \phi^6/6$  [19] have also been extensively studied, subject to the conditions  $b_2 > 27/38$  ( $b_3 > 0$ ) required to guarantee the presence of an interval of coexistence between the homogeneous state  $\phi = 0$  and a spatially periodic state. Note that in the context of nonconserved dynamics [19,46] one generally selects a nonlinear term  $g_{\text{nl}}$  directly, although this term is related to  $f_{\text{nl}}$  through the relation  $g_{\text{nl}} \equiv -df_{\text{nl}}/d\phi$ , i.e.,  $g_{23}$  or  $g_{35}$ .

As we shall see below, in the conserved case, having the nonlinear term  $f_{23}$  describes the generic case and the role of the coefficient  $b_2$  is effectively played by the value of  $\phi_0$ , which is the average value of the order parameter  $\phi(\mathbf{x})$ .

Equation (3) can be studied in one, two, or more dimensions. In one dimension with  $g_{23}$  the equation was studied by Matthews and Cox [37,38] as an example of a system with a conserved order parameter; this equation is equivalent to Eq. (3) with imposed nonzero mean  $\phi$ . A weakly localized state of the type that is of interest in the present paper is computed in Ref. [37] and discussed further in Ref. [38].

### B. Localized states in one spatial dimension

We first consider Eq. (3) in one dimension, with  $\alpha = 1$  and  $q = 1$ , i.e.,

$$\partial_t \phi = \partial_x^2 [r\phi + (\partial_x^2 + 1)^2 \phi + \phi^3]. \quad (4)$$

This equation is reversible in space (i.e., it is invariant under  $x \rightarrow -x$ ). Moreover, it conserves the total “mass”  $\int_0^L \phi dx$ , where  $L$  is the size of the system. In the following, we denote the average value of  $\phi$  in the system by  $\phi_0 \equiv \langle \phi \rangle$  so that perturbations  $\tilde{\phi} \equiv \phi - \phi_0$  necessarily satisfy  $\langle \tilde{\phi} \rangle = 0$ , where  $\langle \dots \rangle \equiv L^{-1} \int_0^L (\dots) dx$ .

Steady states ( $\partial_t \phi = 0$ ) are solutions of the fourth-order ordinary differential equation

$$0 = r\phi + (\partial_x^2 + 1)^2 \phi + \phi^3 - \mu, \quad (5)$$

where  $\mu \equiv \delta F[\phi]/\delta \phi$  is an integration constant that corresponds to the chemical potential.

Each solution of this equation corresponds to a stationary value of the underlying Helmholtz free energy,

$$\tilde{F} = \int_0^L \left[ (1+r) \frac{\phi^2}{2} + \frac{\phi^4}{4} - (\partial_x \phi)^2 + \frac{1}{2} (\partial_{xx} \phi)^2 \right] dx. \quad (6)$$

We use the free energy to define the grand potential

$$\Omega = \tilde{F} - \int_0^L \mu \phi dx \quad (7)$$

and will be interested in the normalized free-energy density  $f = \{\tilde{F}[\phi(x)] - \tilde{F}[\phi_0]\}/L$  and in the density of the grand potential  $\omega = \Omega/L = \tilde{F}[\phi(x)]/L - \mu\phi_0$ . We also use the  $L^2$  norm

$$\|\delta\phi\| = \sqrt{\frac{1}{L} \int_0^L (\phi - \phi_0)^2 dx} \quad (8)$$

as a convenient measure of the amplitude of the departure of the solution from the homogeneous background state  $\phi = \phi_0$ .

Linearizing Eq. (4) about the steady homogeneous solution  $\phi = \phi_0$  using the ansatz  $\delta\phi(x,t) \equiv \phi(x,t) - \phi_0 = \epsilon \exp(\beta t + ikx)$  with  $\epsilon \ll 1$  results in the dispersion relation

$$\beta = -k^2 [r + (1 - k^2)^2 + 3\phi_0^2]. \quad (9)$$

It follows that in an infinite domain, the threshold for instability of the homogeneous state corresponds to  $r_c^\infty = -3\phi_0^2$ . In a domain of finite length  $L$  with periodic boundary conditions (PBC), the homogeneous state is linearly unstable for  $r < r_n$ , where

$$r_n = -(1 - k_n^2)^2 - 3\phi_0^2, \quad (10)$$

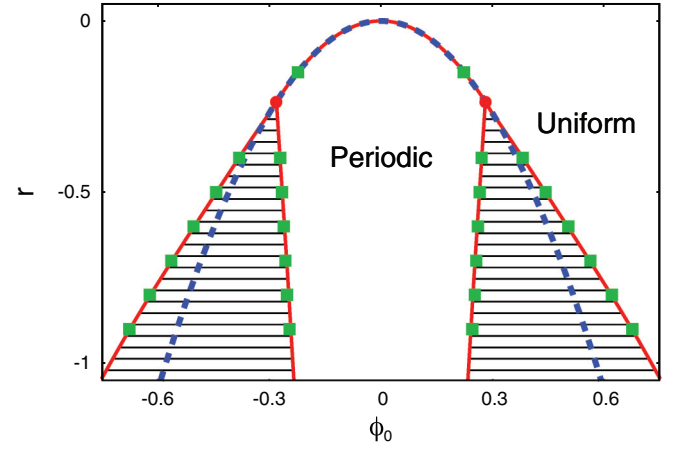


FIG. 1. (Color online) The phase diagram for the 1D PFC model (3) when  $q = 1$ . The red solid lines are the coexistence curves between the periodic and uniform phases calculated using a two-mode approximation [28]. The green squares show the coexistence values calculated from simulations [28]. The red circles are the tricritical points. The blue dashed line shows the curve of marginal stability of the uniform state within linear stability theory.

and  $k_n \equiv 2\pi n/L$ ,  $n = 1, 2, \dots$ . Standard bifurcation theory with PBC shows that for  $L < \infty$  each  $r_n$  corresponds to a bifurcation point creating a branch of periodic solutions that is uniquely specified by the corresponding integer  $n$ . For those integers  $n$  for which  $r_n > -9/2$ , the branch of periodic states bifurcates supercritically (i.e., toward smaller values of  $|\phi_0|$ ); for  $r_n < -9/2$ , the bifurcation is subcritical (i.e., the branch bifurcates toward larger values of  $|\phi_0|$ ). Since each solution can be translated by an arbitrary amount  $d \pmod{L}$ , each bifurcation is in fact a pitchfork of revolution. Although the periodic states can be computed analytically for  $r \approx r_n$ , for larger values of  $|r - r_n|$  numerical computations are necessary. In the following we use the continuation toolbox AUTO [47,48] to perform these (and other) calculations. For interpreting the results it is helpful to think of  $r$  as a temperature-like variable which measures the undercooling of the liquid phase.

Before we can discuss LS in the above model, it is helpful to refer to the phase diagram appropriate to a one-dimensional (1D) setting (Fig. 1). As shown in Ref. [28], the tricritical point is located at  $(\phi_{0b}, r_b^{\max}) = (\pm\sqrt{3/38}, -9/38)$ . For  $r > r_b^{\max}$  there exists no thermodynamic coexistence zone between the homogeneous and periodic states. Such a region is only present for  $r < r_b^{\max}$  and is limited by the binodal lines that indicate the values of  $\phi_0$  for which the homogeneous and periodic solutions at fixed  $r$  have equal chemical potential and pressure (i.e., equal grand potential). Thus for  $r < r_b^{\max}$  the transition from the homogeneous to the periodic state is of first order. The binodals can either be calculated for specific domain sizes and periods of the periodic structure or for an infinite domain. In the latter case, the period of the periodic state is not fixed but corresponds to the period that minimizes the Helmholtz free energy at each  $(\phi_0, r)$  [28]. We remark that with this choice of parameters, the tricritical point is not the point at which the bifurcation to the periodic state changes from supercritical to subcritical. As already mentioned, the latter occurs at  $(\phi_0, r) = (\pm\sqrt{3/2}, -9/2)$ , i.e., at values of  $r$

much smaller than  $r_b^{\max}$ . Further discussion of this point may be found in the Conclusions.

### III. RESULTS FOR THE CONSERVED SWIFT-HOHENBERG EQUATION

#### A. Families of localized states

Since Eq. (4) represents conserved gradient dynamics based on an energy functional that allows for a first-order phase transition between the homogeneous state and a periodic patterned state, one may expect the existence of localized states (LS) to be the norm rather than an exception. In the region between the binodals, where homogeneous and periodic structures may coexist, the value of  $\phi_0$ , i.e., the amount of “mass” in the system, determines how many peaks can form.

As in other problems of this type, we divide the LS into three classes. The first class consists of left-right symmetric structures with a peak in the middle. Structures of this type have an overall odd number of peaks and we shall refer to them as odd states, hereafter  $LS_{\text{odd}}$ . The second class consists of left-right symmetric structures with a dip in the middle. Structures of this type have an overall even number of peaks and we refer to them as even states, hereafter  $LS_{\text{even}}$ . Both types have even parity with respect to reflection in the center of the structure. The third class consists of states of no fixed parity, i.e., asymmetric states,  $LS_{\text{asym}}$ . The asymmetric states are created from the symmetric states at pitchfork bifurcations and take the form of rungs on a ladderlike structure with interconnections between  $LS_{\text{odd}}$  to  $LS_{\text{even}}$ . In view of the gradient structure of Eq. (4), the asymmetric states are likewise stationary solutions of the equation.

We now address the following questions:

- (i) Do localized states exist outside the binodal region? Can they form the energetic minimum outside the binodal region?
- (ii) How does the bifurcational structure of the localized states change with changes in the temperature-like parameter  $r$ ? How does the transition from tilted or slanted snaking to no snaking occur? What is the behavior of the asymmetric localized states during this process?

Answers to these and other questions can be obtained by means of an in-depth parametric study. In the figures that follow, we present bifurcation diagrams for localized states as a function of the mean order parameter value  $\phi_0$  for a number of values of the parameter  $r$ . All are solutions of Eq. (5) that satisfy periodic boundary conditions on the domain  $0 \leq x \leq L$ , and are characterized by their  $L^2$  norm  $\|\delta\phi\|$ , chemical potential  $\mu$ , free-energy density  $f$ , and grand potential density  $\omega$  as defined in Sec. II B.

In Fig. 2 we show the results for  $r = -0.9$  for  $L = 100$ . Figure 2(a) shows  $\|\delta\phi\|$  as a function of  $\phi_0$ : the classical bifurcation diagram. For these parameter values, as  $\phi_0$  is increased the homogeneous (liquid) phase first becomes unstable to perturbations with mode number  $n = 16$  (i.e., 16 bumps), followed closely by bifurcations to modes with  $n = 15$  and 17. All other modes bifurcate at yet smaller values of  $|\phi_0|$  and are omitted. All three primary bifurcations are supercritical. The figure also reveals that the  $n = 16$  branch undergoes a secondary instability already at small amplitude; this instability creates a pair of secondary branches of spatially

localized states,  $LS_{\text{odd}}$  (solid line) and  $LS_{\text{even}}$  (dashed line). With increasing amplitude these branches undergo *slanted snaking* as one would expect on the basis of the results for related systems with a conservation law [21,24]. The  $LS_{\text{odd}}$  and  $LS_{\text{even}}$  branches are in turn connected by ladder branches consisting of asymmetric states  $LS_{\text{asym}}$ , much as in standard snaking [46]. Sample solution profiles for these three types of LS are shown in Fig. 3. The snaking ceases when the LS have grown to fill the available domain; in the present case, the  $LS_{\text{odd}}$  and  $LS_{\text{even}}$  branches terminate on the same  $n = 16$  branch that created them in the first place. Whether or not this is the case depends in general on the domain length  $L$ , as discussed further in Ref. [49].

The key to the bifurcation diagram shown in Fig. 2(a) is evidently the small amplitude bifurcation on the  $n = 16$  branch. This bifurcation destabilizes the  $n = 16$  branch that would otherwise be stable and is a consequence of the presence of the conserved quantity  $\phi_0$  [37]. As  $L$  increases, the bifurcation moves down to smaller and smaller amplitude, so that in the limit  $L \rightarrow \infty$  the periodic branch is entirely unstable and the LS bifurcate directly from the homogeneous state. Since the LS bifurcate *subcritically*, it follows that such states are present not only when the primary pattern-forming branch is supercritical but moreover are present *below* the onset of the primary instability.

Figure 2(b) shows the corresponding plot of the free-energy density  $f$  as a function of  $\phi_0$ . This figure demonstrates that throughout much of the range of  $\phi_0$ , the localized states have a lower free energy than the extended periodic states. In this range, the LS are therefore energetically favored. Figure 2(c) shows the corresponding plot of the chemical potential  $\mu$  while Fig. 2(d) shows the grand potential density  $\omega$ . Of these, Fig. 2(c) is perhaps the most interesting since it shows that the results of Fig. 2(a), when replotted using  $(\phi_0, \mu)$  to characterize the solutions, in fact take the form of standard snaking, provided one takes the chemical potential  $\mu$  as the control parameter and  $\phi_0$  as the response. In this form, the bifurcation diagram gives the values of  $\phi_0$  that are consistent with a given value of the chemical potential  $\mu$  (recall that  $\phi_0$  is related to the total particle number density).

We now show how the bifurcation diagrams evolve as the temperature-like parameter  $r$  changes. We begin by showing the bifurcation diagrams for decreasing values of  $|r|$ . In the Appendix, we use amplitude equations to determine the direction of branching of the localized states. Here we discuss the continuation results.

The bifurcation diagram for  $r = -0.7$  [Figs. 4(a) and 4(b)] resembles that for  $r = -0.9$  (Fig. 2) although the snaking structure has moved toward smaller  $|\phi_0|$  and is now thinner. In addition, it is now the second saddle node on the  $LS_{\text{odd}}$  branch that lies farthest to the left, and not the first. For  $r = -0.6$  [Figs. 4(c) and 4(d)], the branches of localized states still form a tilted snakes-and-ladders structure, but the saddle nodes on the  $LS_{\text{odd}}$  and  $LS_{\text{even}}$  branches are now absent, i.e., both solution branches now grow monotonically. The resulting diagram has been called “smooth snaking” [50]. However, despite the absence of the saddle nodes on the  $LS_{\text{odd}}$  and  $LS_{\text{even}}$  branches, the interconnecting ladder states consisting of asymmetric states still remain. This continues to be the case when  $r = -0.5$  [Figs. 4(e) and 4(f)] although the structure



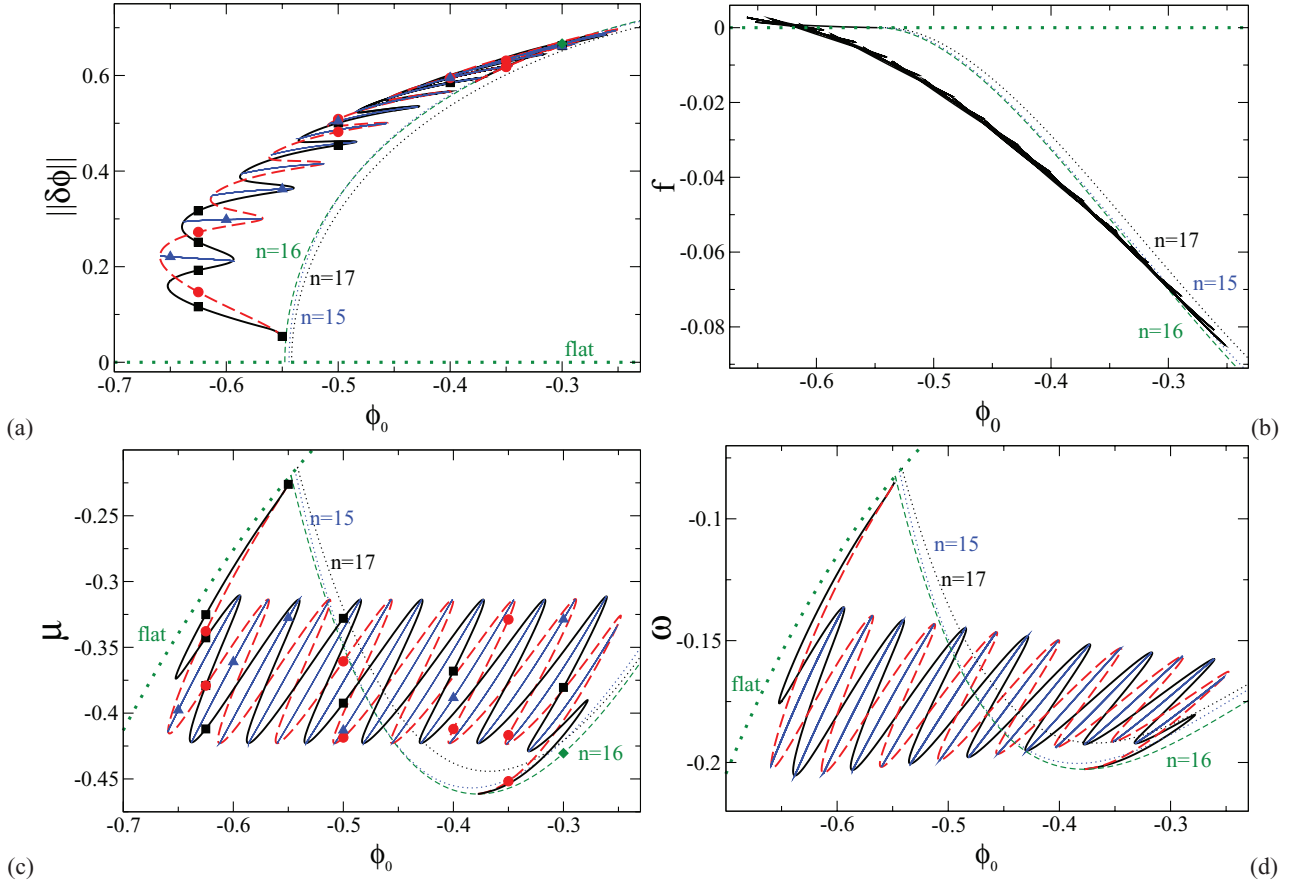


FIG. 2. (Color online) Characteristics of steady-state (localized) solutions of the one-dimensional conserved Swift-Hohenberg equation (4) as a function of the mean order parameter  $\phi_0$  for a fixed domain size of  $L = 100$  and  $r = -0.9$ . The various solution profiles are characterized by their (a)  $L^2$  norm  $\|\delta\phi\|$ , (b) free-energy density  $f$ , (c) chemical potential  $\mu$ , and (d) grand potential density  $\omega$ . The thick green dotted line, labeled “flat,” corresponds to the homogeneous solution  $\phi(x) = \phi_0$ . Periodic solutions with  $n = 16$  peaks are shown as a thin green dashed line, whereas the nearby thin blue and black dotted lines represent the  $n = 15$  and  $17$  solutions, respectively. The thick solid black and dashed red lines that bifurcate from the  $n = 16$  periodic solution represent symmetric localized states with a maximum ( $LS_{\text{odd}}$ ) and a minimum ( $LS_{\text{even}}$ ) at their center, respectively. Both terminate on the  $n = 16$  solution. The 14 blue solid lines that connect the  $LS_{\text{odd}}$  and  $LS_{\text{even}}$  branches of symmetric localized states correspond to asymmetric localized states ( $LS_{\text{asym}}$ ). Together these three sets of branches of localized states form a tilted snakes-and-ladders structure. Typical order parameter profiles along the three LS branches are shown in Fig. 3 and correspond to locations indicated in panels (a) and (c) by filled black squares ( $LS_{\text{odd}}$ ), red circles ( $LS_{\text{even}}$ ), blue triangles ( $LS_{\text{asym}}$ ), and green diamond (periodic solution with  $n = 16$ ).

has moved to yet smaller  $|\phi_0|$  and the snake has become even thinner. Finally, for  $r = -0.4$  [Figs. 4(g) and 4(h)], the snake is nearly dead, and only tiny wiggles remain. The bifurcation of the localized states from the  $n = 16$  periodic state is now supercritical (see the Appendix) but the LS branches continue to terminate on the same branch at larger amplitude, and do so via a single saddle node at the right [Fig. 4(h)]. Sample profiles along the resulting  $LS_{\text{odd}}$  branches are shown for several values of  $r$  in Fig. 5. We note that a change of  $r$  has a profound effect on the transition region between the homogeneous background state and the periodic state: with decreasing  $|r|$  the LS become wider and the localized periodic structure looks more and more like a wave packet with a smooth sinusoidal modulation of the peak amplitude.

As the “temperature”  $r$  decreases below  $r = -0.9$ , the bifurcation diagrams remain similar to those displayed in Fig. 2 until just before  $r = -1.5$ , where substantial changes take place and the complexity of the bifurcation diagram grows dramatically. This is a consequence of the appearance of other

types of localized states that we do not discuss here. Likewise, we omit here all bound states of the LS described above. These are normally found on an infinite stack of isolas that are also present in the snaking region [51,52].

### B. Tracking the snake

In Fig. 6 we show, for  $-1.5 < r < -0.4$ , the result of tracking *all* the saddle-node bifurcations visible in the previous bifurcation diagrams in the  $(\phi_0, r)$  plane, while Fig. 7 shows an enlargement of the region  $-0.8 < r < -0.3$  together with the result of tracking the tertiary pitchfork bifurcations to the asymmetric states.

Figure 6 shows that the saddle nodes annihilate pairwise in cusps as  $r$  increases. The annihilations occur first for smaller  $\phi_0$  and later for larger  $\phi_0$ , and occur alternately on  $LS_{\text{odd}}$  and  $LS_{\text{even}}$ . Above the locus of the cusps the snaking is smooth, although as shown in Fig. 7 the tertiary ladder states remain. The thick green curve in Fig. 7 represents the locus of the secondary bifurcation from the  $n = 16$  periodic state to LS and

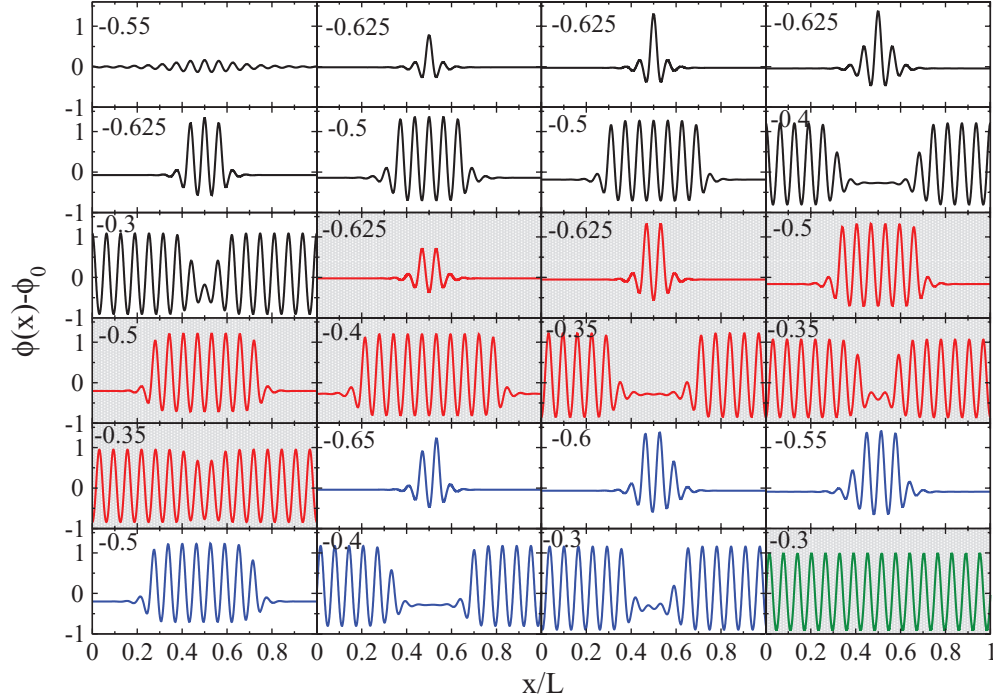


FIG. 3. (Color online) A selection of steady-state profiles  $\phi(x) - \phi_0$  for  $r = -0.9$  and values of  $\phi_0$  in the range  $-0.65 \leq \phi_0 \leq -0.3$  (the number in each panel indicates the corresponding value of  $\phi_0$ ). Going from top left to bottom right, we first show nine  $\text{LS}_{\text{odd}}$  solutions, i.e., symmetric localized states with an odd number of maxima (in black), then eight  $\text{LS}_{\text{even}}$  solutions, i.e., symmetric localized states with an even number of maxima (in red), followed by six  $\text{LS}_{\text{asym}}$  solutions, i.e., asymmetric localized states (in green). The final plot is the  $n = 16$  periodic solution for  $\phi_0 = -0.3$  (in blue). The solutions on the symmetric branches correspond to locations indicated in Fig. 2(a) and are shown in order, starting from the left bifurcation point that creates them and continuing to larger norm  $\|\delta\phi\|$ . The color coding corresponds to that used in Figs. 2(a) and 2(c):  $\text{LS}_{\text{odd}}$  (filled black squares),  $\text{LS}_{\text{even}}$  (red circles),  $\text{LS}_{\text{asym}}$  (blue triangles), and periodic (green diamond).

shows that on either side the bifurcation to LS is subcritical for sufficiently negative  $r$  but becomes supercritical at larger  $r$ , cf. Fig. 4(h) and the Appendix.

One may distinguish six intervals in  $r$  with different types of behavior. These depend on the system size, but the results in Fig. 7 for  $L = 100$  are representative:

(i) For  $r > -0.33$ : no LS exist, the only nontrivial states are periodic solutions.

(ii) For  $-0.33 > r > -0.39$ : branches of even and odd symmetric LS are present, and appear and disappear via supercritical secondary bifurcations from the branch of periodic solutions. With decreasing  $r$ , more and more branches of asymmetric LS emerge from these two secondary bifurcation points.

(iii) For  $-0.39 > r > -0.41$ : both branches of symmetric LS emerge subcritically at large  $\phi_0$  and supercritically at small  $\phi_0$ .

(iv) For  $-0.41 > r > -0.56$ : both branches of symmetric LS emerge subcritically at either end. Further branches of asymmetric LS emerge with decreasing  $r$  either from the two secondary bifurcation points or from the saddle-node bifurcations on the branches of symmetric LS, but the symmetric LS still do not exhibit snaking, i.e., no additional folds are present on the branches of symmetric LS.

(v) For  $-0.56 > r > -0.64$  (highlighted by the gray shading in Fig. 7): pairs of saddle nodes appear successively in cusps as  $r$  decreases, starting at larger  $\phi_0$ . Thereafter, saddle

nodes appear alternately on branches of even and odd symmetric LS. The appearance of the cusps is therefore associated with the transition from smooth snaking to slanted snaking.

(vi) For  $-0.64 > r$ : the slanted snake is fully developed. Only one further pair of saddle-node bifurcations appears in the parameter region shown in Fig. 7. With decreasing  $r$  the snaking becomes stronger; each line in Figs. 6 and 7 that represents a saddle-node bifurcation crosses more and more other such lines, i.e., more and more different states are possible at the same values of  $\phi_0$ . Furthermore, the subcritical regions (outside the green curve in Fig. 7) become larger.

### C. Relation to binodal lines

From the condensed-matter point of view, where the cSH/PFC equation represents a model for the liquid (homogeneous) and solid (periodic) phases, one is particularly interested in results in the thermodynamic limit  $L \rightarrow \infty$ . As mentioned above in the context of the phase diagram in Fig. 1, the binodal lines correspond to values of  $(\phi_0, r)$  at which the homogeneous state and the minimum energy periodic state coexist in the thermodynamic limit. These are defined as pairs of points at which the homogeneous state and the periodic state have the same “temperature” (i.e., same  $r$  value), the same chemical potential  $\mu$ , and the same pressure  $p = -\omega$ , and are displayed as the blue dash-dot lines in Fig. 8. For a given value of  $r$ , these two lines give the values of  $\phi_0$  of the coexisting

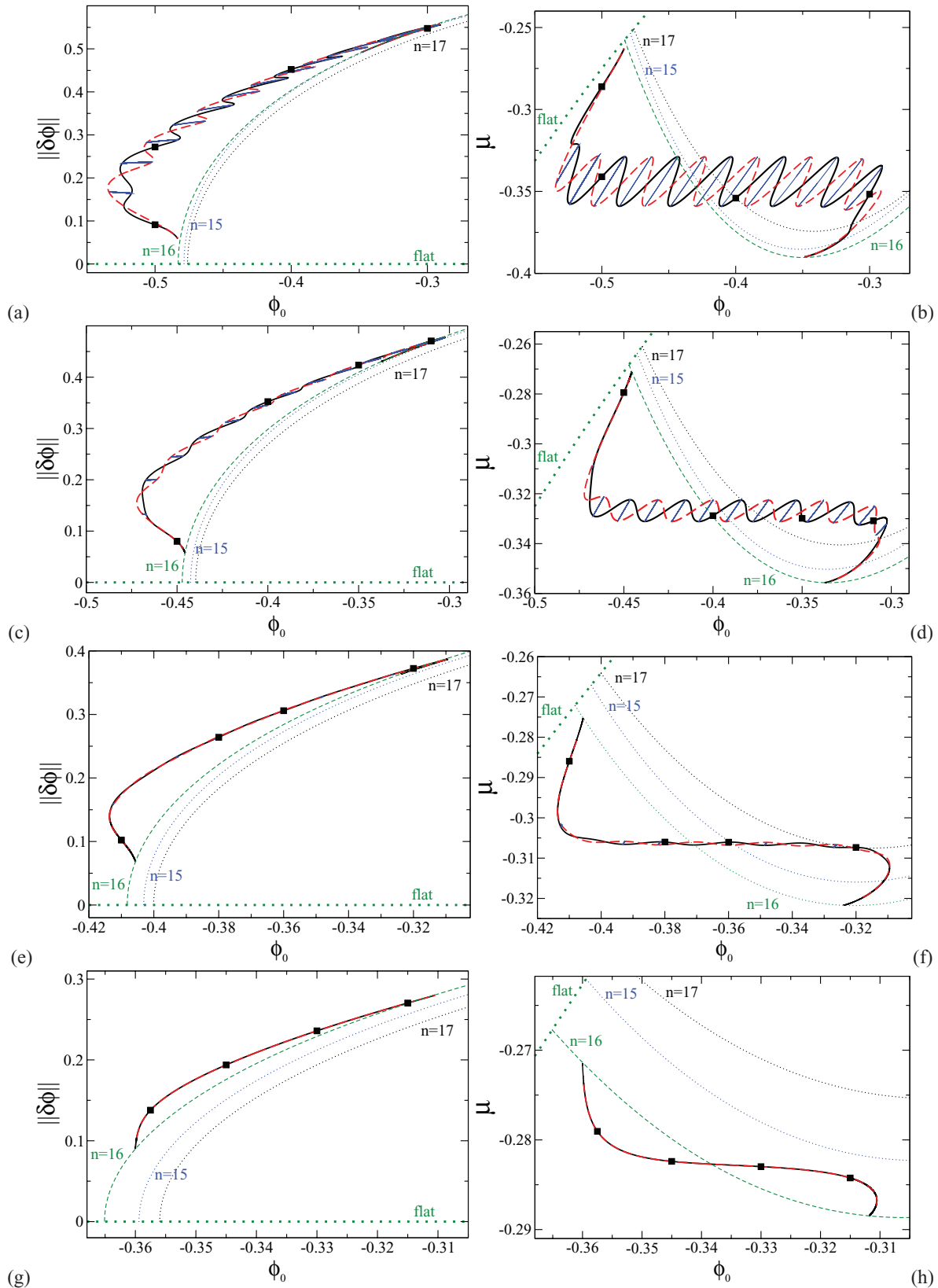


FIG. 4. (Color online) The norm (left) and chemical potential (right) of the homogeneous, periodic, and localized steady-state solutions as a function of the mean order parameter  $\phi_0$ , for a fixed domain size of  $L = 100$  and several values of  $r > -0.9$ : (a) and (b)  $r = -0.7$ , (c) and (d)  $r = -0.6$ , (e) and (f)  $r = -0.5$ , and (g) and (h)  $r = -0.4$ . The line styles are as in Fig. 2. Typical order parameter profiles along the branches of symmetric localized states with an odd number of maxima (black lines) are shown in Fig. 5 and correspond to locations indicated in the panels by filled black squares.

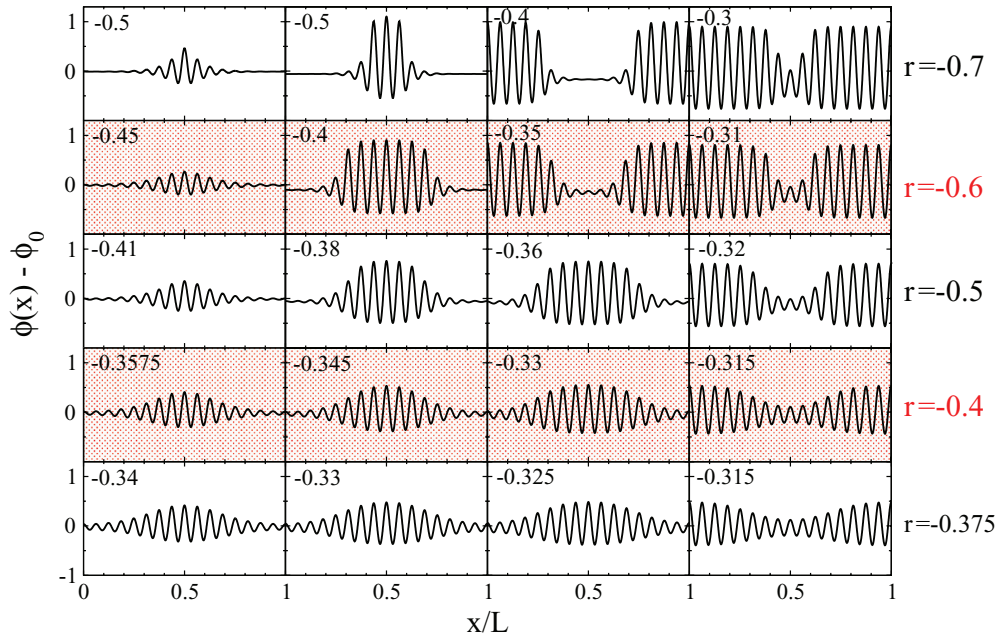


FIG. 5. (Color online) A selection of steady-state profiles  $\phi(x) - \phi_0$  along the  $LS_{\text{odd}}$  branches shown in Fig. 4 for  $r = -0.7$  (first row),  $r = -0.6$  (second row),  $r = -0.5$  (third row),  $r = -0.4$  (fourth row), and  $r = -0.375$  (last row), for various values of  $\phi_0$ , as indicated in the top left corner of each panel. The solutions in each row are shown in order, starting from near the left bifurcation point that creates them and continuing to larger norm  $\|\delta\phi\|$ . The locations of the profiles are indicated in Fig. 4 by the filled black squares. The bifurcation diagram for  $r = -0.375$  (not shown in Fig. 4) is qualitatively the same as that for  $r = -0.4$ .

homogeneous (lower  $\phi_0$ ) and periodic (higher  $\phi_0$ ) states. Note that when plotted with the resolution of Fig. 8, the binodals are indistinguishable from the coexistence lines between the finite size ( $L = 100$ )  $n = 16$  periodic solution and the homogeneous state. Figure 8 also displays the line (green solid line) at which the  $L = 100$  localized states bifurcate from the  $n = 16$  branch of periodic solutions. For  $r < -0.41$ , the LS bifurcations are subcritical implying that the localized states are present outside the green solid line. Figure 8 shows the loci of the outermost saddle-node bifurcations on the branches of symmetric LS

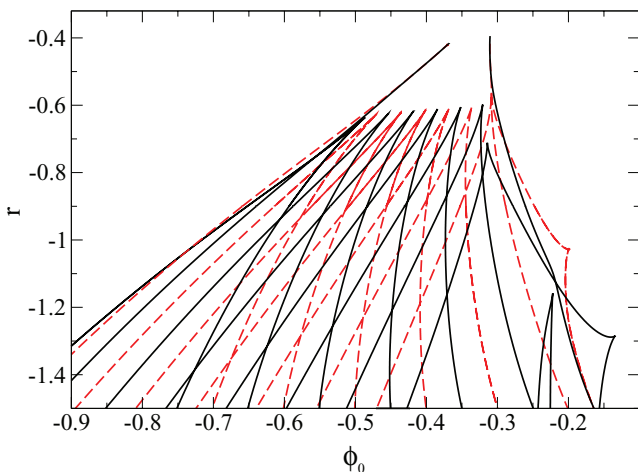


FIG. 6. (Color online) Loci of saddle-node bifurcations on the branches of symmetric localized states in the  $(\phi_0, r)$  plane for  $r > -1.5$ . Saddle nodes annihilate pairwise as  $r$  increases (solid black lines,  $LS_{\text{odd}}$ ; dashed red lines,  $LS_{\text{even}}$ ).

that result (dashed lines to the left and to the right of the green solid line for  $r < -0.41$ ). The most striking aspect of Fig. 8 is that for  $r \lesssim -1$  these lines actually cross and exit the region between the two binodal lines, indicating that in the one-dimensional PFC model one can find stable LS *outside*

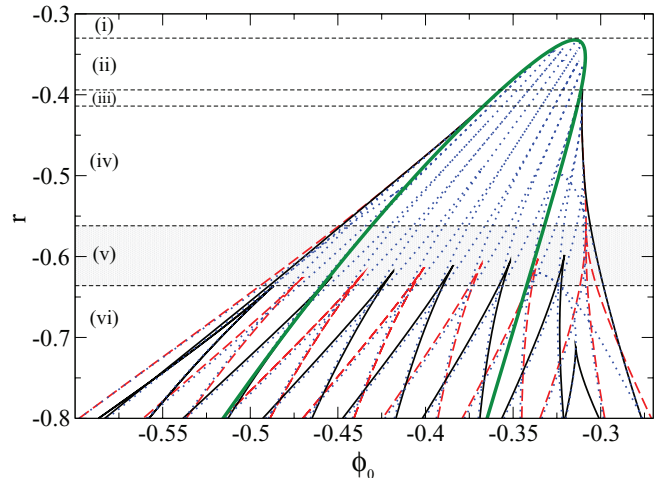


FIG. 7. (Color online) Loci of the saddle-node bifurcations on the branches of symmetric localized states in the  $(\phi_0, r)$  plane (solid black lines:  $LS_{\text{odd}}$ ; dashed red lines:  $LS_{\text{even}}$ ) together with the bifurcations to asymmetric localized states (dotted blue lines) for  $r > -0.8$ . The thick green curve represents the locus of secondary bifurcation from the periodic  $n = 16$  state to localized states and shows that on either side the bifurcation to LS is subcritical for sufficiently negative  $r$  but becomes supercritical at larger  $r$ .



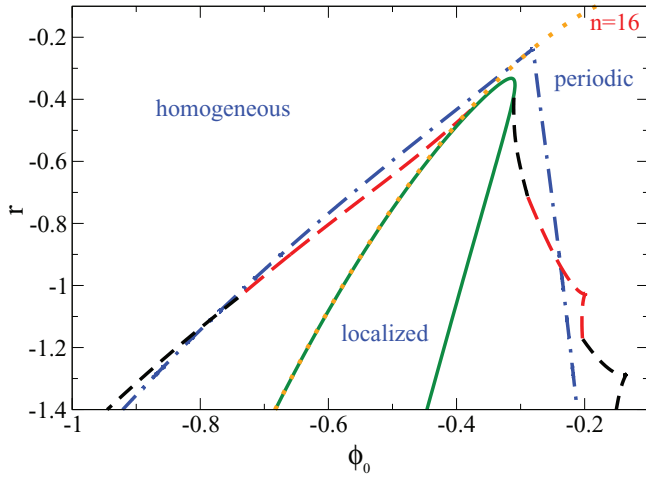


FIG. 8. (Color online) Loci in the  $(\phi_0, r)$  plane computed for  $L = 100$  of (i) the primary bifurcation from the homogeneous state to the  $n = 16$  periodic branch (dotted orange line); (ii) the bifurcation of the localized states from the  $n = 16$  periodic branch (solid green line); (iii) the outermost saddle-node bifurcations on the branches of symmetric localized states (long-dashed red and short-dashed black lines); and (iv) the binodals between the periodic and homogeneous states (dot-dashed blue lines). The latter coincide with the binodals for the  $n = 16$  periodic state and the homogeneous state to within the resolution of the figure. Figures 6 and 7 show how the loci of the outermost saddle-node bifurcations of localized states fit into the overall picture.

of the binodal. Although these are not the lowest free-energy states (we have checked this for  $r \gtrsim -1.5$ ), this remarkable fact points toward the possibility of metastable nanocrystals existing outside of the binodal. We must mention, however, that these structures have only been found in one spatial dimension, in a finite-size system with  $L = 100$ ; we have not investigated their properties for larger system sizes  $L$  and specifically in the thermodynamic limit  $L \rightarrow \infty$ .

**D. Stability**

For applications it is also necessary to know the stability properties of the localized solutions we have computed. Although we have not determined the stability properties of every solution, we have used numerical continuation of the linear stability problem to examine the stability properties of the symmetric localized states in two of the most interesting cases,  $r = -0.9$  and  $-0.6$ . In the former case, the system exhibits slanted snaking while in the latter the snaking is smooth. The combination of these results suffices to determine the stability assignments in the remaining cases, including those for the asymmetric rung states.

The results are displayed in Fig. 9. The figure shows how the two leading eigenvalues change along the branches of symmetric localized states. Figures 9(a) and 9(c) show, respectively, the results for the even symmetric state  $LS_{\text{even}}$  (dashed lines) and the odd symmetric state  $LS_{\text{odd}}$  (solid lines) for  $r = -0.9$  [cf. Fig. 2(a)]. In each case, the thick lines show the amplitude eigenvalue while the thin lines show the symmetry-breaking phase eigenvalue, referred to as the symmetric and asymmetric

modes, respectively. The figures should be read from point A representing the beginning of the snaking branch at small amplitude to point B representing the termination of the branch. Figure 9(a) shows that the even states  $LS_{\text{even}}$  are initially doubly unstable: both eigenvalues are positive. Both cross zero almost simultaneously at the leftmost saddle node in the same manner as in standard homoclinic snaking [46] and thereafter perform in-phase gyrations until the rightmost saddle node. These gyrations imply that the  $LS_{\text{even}}$  states are stable between adjacent saddle nodes, specifically between the first and second saddle nodes, the third and fourth saddle nodes, etc., again as in standard homoclinic snaking. Both eigenvalues execute essentially identical motion, except near A, where the amplitude eigenvalue is  $O(1)$  and positive while the phase eigenvalue is very small (indeed, exponentially small, if the problem is posed on the real line), and near B where both eigenvalues are also positive, with an  $O(1)$  amplitude eigenvalue and a small phase eigenvalue. Thus the  $LS_{\text{even}}$  states are amplitude and phase-unstable near both A and B, below the nearest saddle node. The reason the two eigenvalues behave in an almost identical manner between the leftmost and rightmost saddle nodes can be traced to the fact that the corresponding eigenfunctions (not shown) are localized at the two fronts at either end of the structure that connect the periodic state in between to the background homogeneous state. When the localized structure is sufficiently long but still narrower than the imposed spatial period, these fronts are only coupled by exponentially small terms in the length of the structure [53]. Thus the fronts are essentially independent and hence the symmetric and antisymmetric modes are almost degenerate [54]. This is again as in standard homoclinic snaking [46]. Figure 9(c) shows that the odd localized states  $LS_{\text{odd}}$  of moderate length behave the same way, except that the phase eigenvalues near A and B are both negative. In particular, the  $LS_{\text{odd}}$  states are also stable between the first and second saddle nodes, the third and fourth saddle nodes, etc. However, the amplitude and phase eigenvalues behave differently near the leftmost saddle node where the structure is very short and near the rightmost saddle node where the domain is almost full. The net outcome of these stability assignments is that the positive slope segments on both branches are stable while the negative slope segments are unstable. Since these overlap there is always at least one stable solution for every value of  $\phi_0$ . Moreover, a careful examination of Figs. 9(a) and 9(c) reveals that the phase eigenvalue always becomes unstable slightly before the amplitude eigenvalue. Thus the stable portions of the branches do not extend all the way to the next saddle node and the asymmetric states bifurcate from amplitude-stable segments, in contrast to the nonconserved Swift-Hohenberg equation [46]. However, these bifurcations are subcritical at both ends (backward relative to the stable portion of the branch from which they bifurcate), implying that the asymmetric states are always unstable—as in the nonconserved Swift-Hohenberg equation [46].

Figures 9(b) and 9(d) show the corresponding results for  $r = -0.6$  [cf. Fig. 4(c)]. Here the amplitude eigenvalue does not generate instabilities except between A and the nearest saddle node and between B and the nearest saddle node. Everywhere else it remains negative. For the  $LS_{\text{even}}$  states, the phase eigenvalue is positive near A but negative near

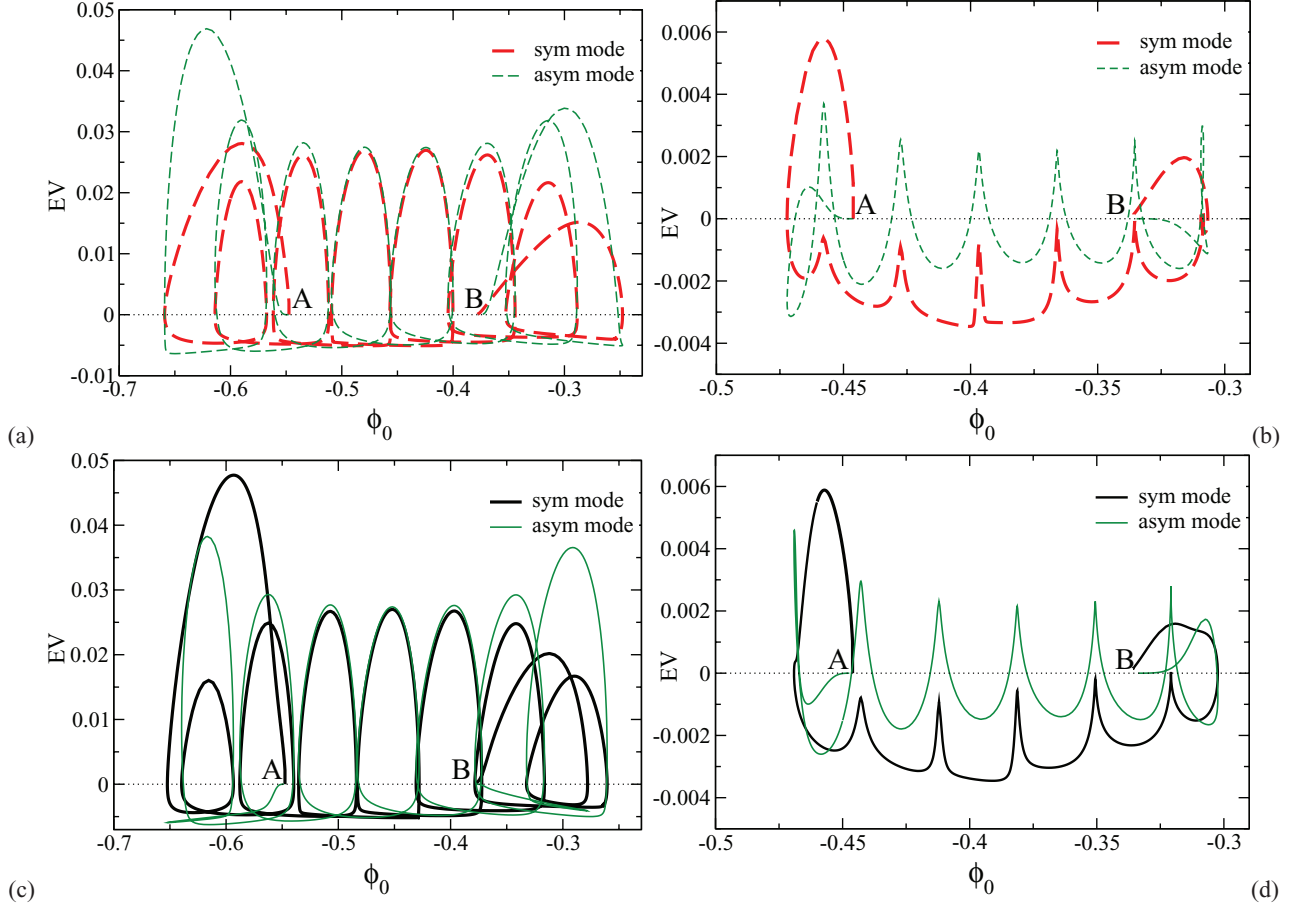


FIG. 9. (Color online) The leading amplitude (thick lines) and phase (thin lines) eigenvalues along the branches of even symmetric states  $LS_{\text{even}}$  (dashed lines) and odd symmetric states  $LS_{\text{odd}}$  (solid lines) for  $r = -0.9$ , displayed in (a) and (c), respectively, and  $r = -0.6$ , displayed in (b) and (d), respectively, computed on a domain of length  $L = 100$ . The remaining eigenvalues are all negative.

B and vice versa for the odd states. In both cases, the phase eigenvalue repeatedly triggers instability but in contrast to  $r = -0.9$  neither eigenvalue executes loops; instead one finds cusplike structures leading to much reduced intervals of instability in comparison with the  $r = -0.9$  case. The results show that the  $LS_{\text{even}}$  states are stable above the leftmost saddle node, lose stability at the next rung, regain it at the following rung, etc. The  $LS_{\text{odd}}$  states, in contrast, are unstable above the leftmost saddle node and acquire stability only at the next rung state before losing it again at the next rung after that. The net outcome of these stability assignments is that the smaller slope segments on both branches are stable while the steeper segments are unstable. Since these overlap, there is always at least one stable solution for every value of  $\phi_0$ . Moreover, as in the  $r = -0.9$  case, the bifurcations to the rung states are subcritical pitchforks at both ends, implying that the asymmetric rung states are unstable throughout.

We emphasize that these stability assignments have been computed at fixed  $\phi_0$ , with  $\phi_0$  varied quasistatically. The stability assignments in the case in which the chemical potential  $\mu$  is fixed and  $\phi_0$  becomes the response [as in Fig. 2(c) or 4(d)] are quite different and, we surmise, identical to those familiar from standard homoclinic snaking.

#### IV. LOCALIZED STATES IN TWO AND THREE DIMENSIONS

##### A. Numerical algorithm

To perform direct numerical simulations (DNS) of the conserved Swift-Hohenberg equation in higher dimensions, we use a recently proposed algorithm [55] that has been proved to be unconditionally energy-stable. As a consequence, the algorithm produces free-energy-decreasing discrete solutions, irrespective of the time step and the mesh size, thereby respecting the thermodynamics of the model even for coarse discretizations. For the spatial discretization, we employ isogeometric analysis [56], which is a generalization of the finite element method. The key idea behind isogeometric analysis is the use of nonuniform rational B-splines (NURBS) instead of the standard piecewise polynomials used in the finite element method. With NURBS, isogeometric analysis gains several advantages over the finite element method. In the context of the conserved Swift-Hohenberg equation, the most relevant one is that the isogeometric analysis permits the generation of arbitrarily smooth basis functions that lead to a straightforward discretization of the higher-order partial derivatives of the conserved Swift-Hohenberg equation [57]. For the time discretization, we use an algorithm especially

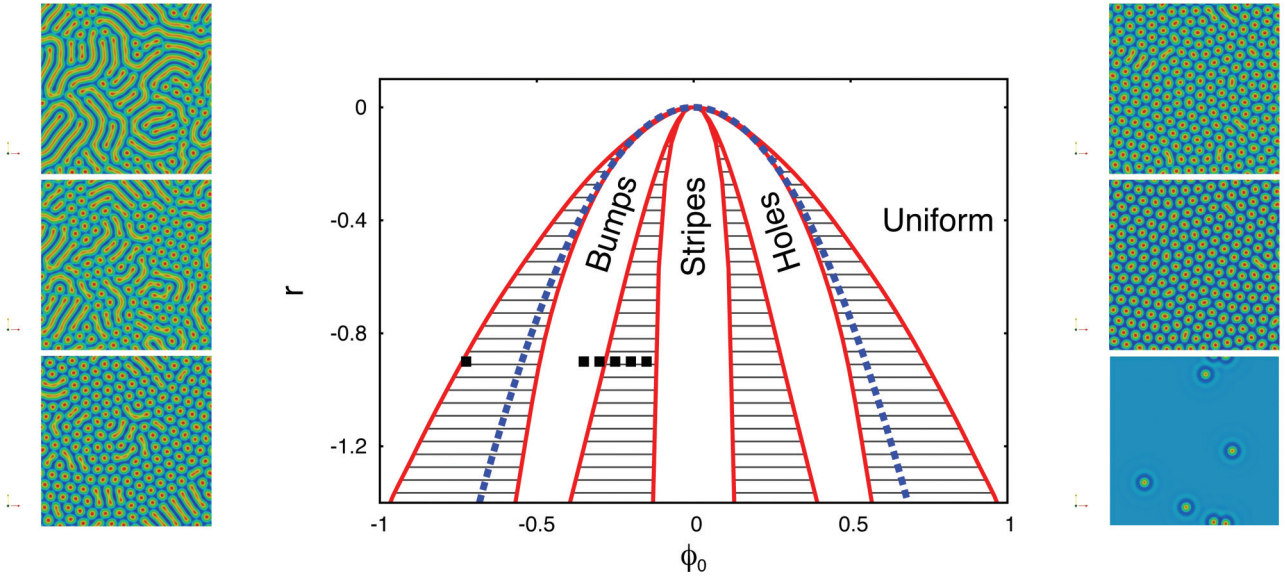


FIG. 10. (Color online) Phase diagram for the conserved Swift-Hohenberg equation, Eq. (3), in two dimensions when  $q = 1$ . The red solid lines show the various coexistence curves, the blue dotted line shows the limit of linear stability, and the gray striped areas show phase coexistence regions. The small panels show steady solutions at  $r = -0.9$  and selected mean order parameter values  $\phi_0$  indicated by the black squares. From top to bottom left  $\phi_0 = -0.15, -0.2$ , and  $-0.25$ , while from top to bottom right  $\phi_0 = -0.3, -0.35$ , and  $-0.725$ . Additional solutions that detail the transition occurring between the last two panels are shown in Fig. 11. The domain size is  $100 \times 100$ .

designed for the conserved Swift-Hohenberg equation. It may be thought of as a second-order perturbation of the trapezoidal rule which achieves unconditional stability, in contrast with the trapezoidal scheme. All details about the numerical algorithms may be found in Ref. [55].

### B. Two dimensions

As in one spatial dimension, the phase diagram for two-dimensional structures helps us to identify suitable parameter values where LS are likely to occur. The phase diagram in Fig. 10, determined numerically [28], shows three distinct phases, labeled “bumps,” “stripes,” and “holes.” In view of the fact that  $\phi(x) = \phi_0 + \delta\phi(x)$ , bumps and holes correspond to perturbations  $\delta\phi(x)$  with opposite signs; both have hexagonal coordination. In addition, the phase diagram reveals four regions of thermodynamic coexistence (hatched in Fig. 10): between bumps and the uniform state, between bumps and stripes, between stripes and holes, and between holes and the uniform state, respectively.

Examples of results obtained by DNS of Eq. (3) starting from random initial conditions are displayed in the side panels of Fig. 10. These six panels show results for fixed  $r = -0.9$ . For small values of  $|\phi_0|$ , the system forms a labyrinthine lamellar-like stripe state; the stripes pinch off locally into bumps as  $|\phi_0|$  is increased, leading to the formation of inclusions of bumps in a background stripe state. The pinching tends to occur first at the ends of a stripe and then proceeds gradually inward. In other cases, free ends are created by the splitting of a stripe into two in a region of high curvature. The formation of bumps tends to take place at grain boundaries, and once bump formation starts, it tends to spread outward from the initial site. For  $\phi_0 = -0.2$ , the areas covered by stripes and bumps are comparable and for larger values of  $|\phi_0|$  the bump

state dominates. By  $\phi_0 = -0.3$  the stripes are almost entirely gone and the state takes the form of a crystalline solid with hexagonal coordination but having numerous defects. As  $|\phi_0|$  increases further, vacancies appear in the solid matrix and for large enough  $|\phi_0|$  the solid “melts” into individual bumps or smaller clusters, as further detailed in Fig. 11.

Figure 11 shows further results from a scan through decreasing values of  $\phi_0$  at  $r = -0.9$ . We focus on the relatively small range  $\phi_0 = -0.45$  to  $-0.675$ , where localized states occur. These reveal a gradual transition from a densely packed solid-like structure to states with a progressively increasing domain area that is free of bumps, i.e., containing the homogeneous state. The bumps percolate through the domain until approximately  $\phi_0 = -0.575$ . For smaller values of  $\phi_0$ , the order parameter profiles resemble a suspension of solid fragments in a liquid phase; the solid is no longer connected. As  $\phi_0$  decreases further, the characteristic size of the solid fragments decreases as the solid fraction falls.

### C. Three dimensions

In three dimensions, Eq. (3) exhibits a large number of steady-state spatially periodic structures. These include those with the symmetries of the simple cubic lattice, the face-centered-cubic lattice, and the body-centered-cubic lattice [58]. Although we do not calculate the phase diagram for the three-dimensional (3D) system, numerical simulations in three dimensions reveal that a lamellar (parallel “sheets”) state is energetically preferred for small  $\phi_0$ . Slices through these structures resemble the stripes observed in two dimensions. As  $|\phi_0|$  increases, the lamellae pinch off, much as in two dimensions, and progressively generate a 3D disordered array of bumps (Fig. 12). This solid-like state is far from being a perfect crystal, however, and with increased  $|\phi_0|$  it develops



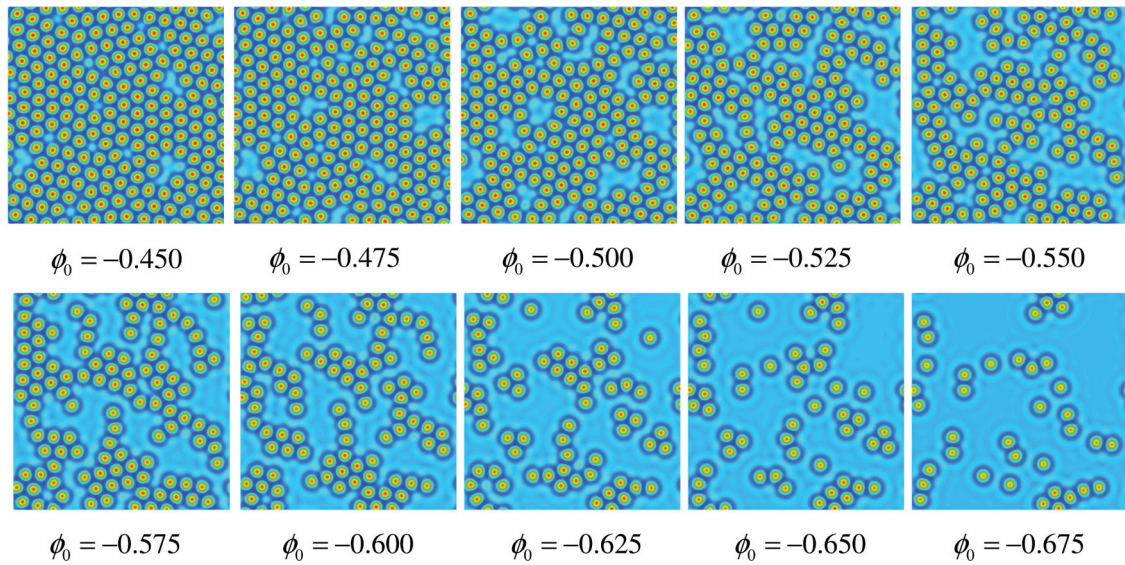


FIG. 11. (Color online) Steady-state solutions of the conserved Swift-Hohenberg equation (3), in two dimensions for  $r = -0.9$  and different mean order parameter values  $\phi_0$  in the range  $-0.675 < \phi_0 < -0.45$ , where localized states occur. The corresponding value of  $\phi_0$  is indicated below each panel. The domain size is  $100 \times 100$ .

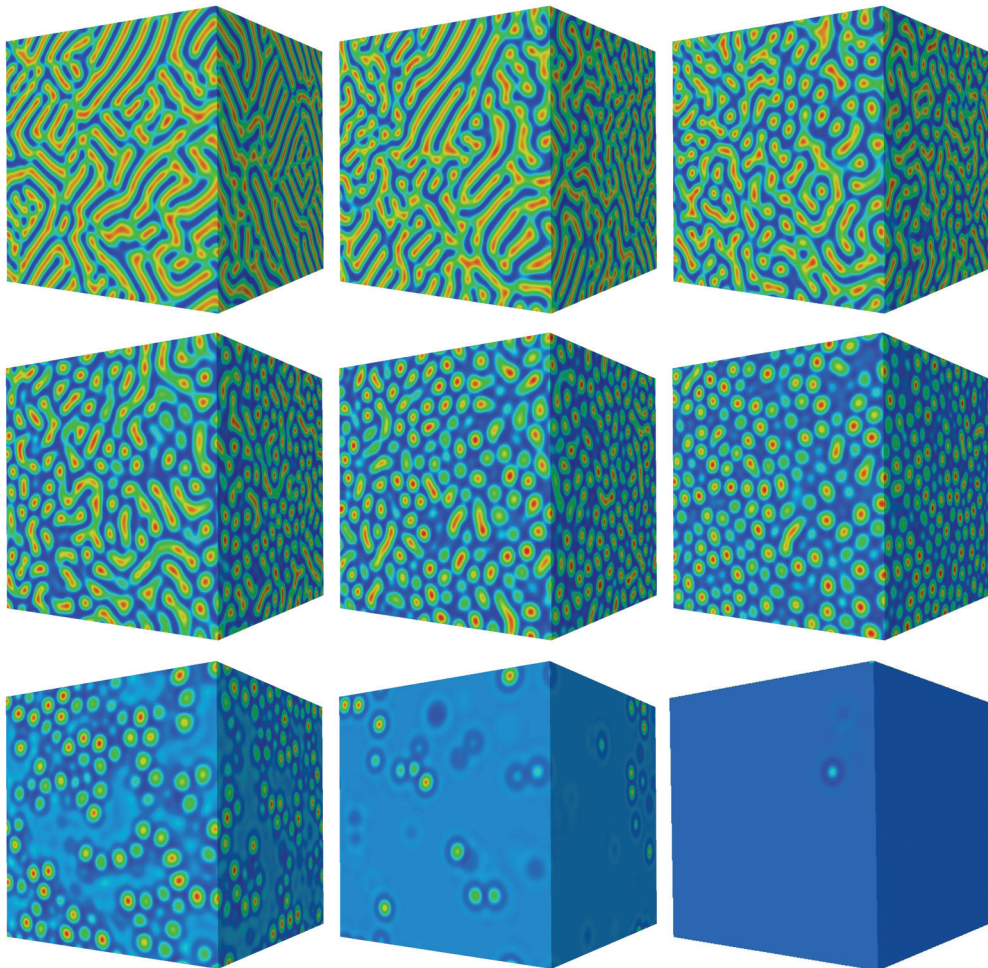


FIG. 12. (Color online) Steady-state localized solutions of Eq. (3) in three dimensions for  $r = -0.9$  and different mean order parameter values  $\phi_0$ : from top left to bottom right  $\phi_0 = -0.025, -0.125, -0.225, -0.325, -0.425, -0.525, -0.625, -0.725$ , and  $-0.750$ . The domain size is  $100 \times 100 \times 100$ .



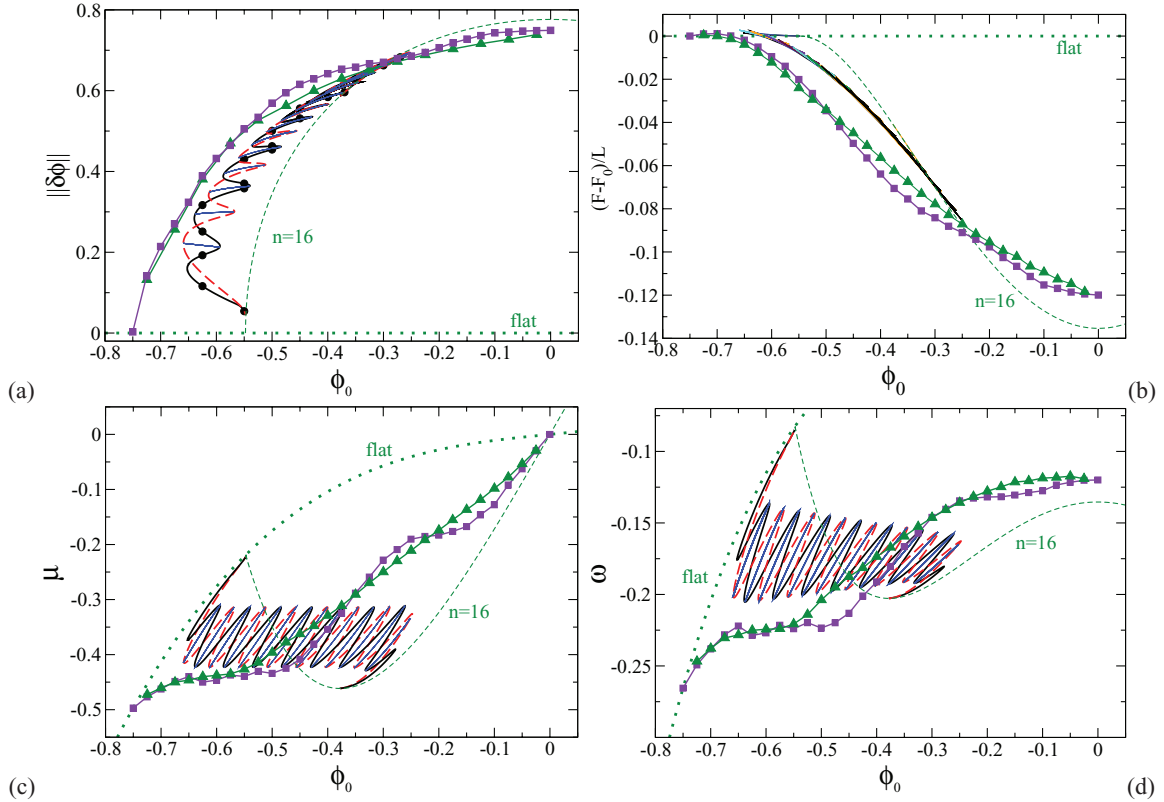


FIG. 13. (Color online) Characteristics of steady-state localized solutions of the conserved Swift-Hohenberg equation for  $r = -0.9$  as a function of the mean order parameter  $\phi_0$  on fixed one, two, and three-dimensional domains of size  $L^d$ ,  $d = 1, 2, 3$ , and  $L = 100$ . The various solution profiles are characterized by their (a)  $L^2$  norm  $\|\delta\phi\|$ , (b) chemical potential  $\mu$ , (c) mean free energy  $(F - F_0)/L^d$ , and (d) mean grand potential  $\omega = F/L^d - \phi_0\mu$ . The connected (violet) square and (green) triangle symbols correspond to 2D calculations (for sample profiles, see Figs. 10 and 11) and 3D calculations (for sample profiles, see Fig. 12). For comparison, we also show the 1D results from Fig. 2 for the periodic (i.e., stripe) state with  $n = 16$  bumps (green dashed line) and the various 1D localized states. The thick green dotted line corresponds to the homogeneous solution  $\phi(\mathbf{x}) = \phi_0$ .

vacancies which eventually lead to its dissolution, just as in two dimensions.

In Fig. 13, we superpose the 2D and 3D DNS results for  $r = -0.9$  on the 1D bifurcation diagrams for  $r = -0.9$  and system size  $L = 100$  (Fig. 2). The 2D order parameter profiles are calculated on a domain with area  $L^2 = 100^2$  and the 3D results have a system volume  $L^3 = 100^3$ . In Fig. 13(a) we display the norm  $\|\delta\phi\|$ , in (b) the chemical potential  $\mu$ , in (c) the mean free energy  $(F - F_0)/L^d$ , and in (d) the mean grand potential  $\omega = F/L^d - \phi_0\mu$ . In each plot the connected (violet) squares correspond to results from 2D calculations such as those displayed in Figs. 10 and 11 and the connected green triangles correspond to 3D results such as those displayed in Fig. 12. It is from examining the figures in panels (c) and (d) that one can most easily discern the reason for the main differences between the 1D results and the 2D and 3D results: we see (particularly in the 2D results) that the chemical potential  $\mu$  and the pressure  $p = -\omega$  have regions where these measures are roughly flat as a function of  $\phi_0$  and regions where they increase as a function of  $\phi_0$ . We also see that these increases in some places relate to features in the 1D results but in other places they do not have any relation to what one sees from the 1D results. This is because in two and three dimensions the system displays phases that are not

seen in one dimension (cf. Figs. 1 and 10). To understand the origin of these roughly flat portions, we recall that in the thermodynamic limit  $L \rightarrow \infty$  two states are said to be at coexistence if the “temperature”  $r$ , the chemical potential  $\mu$ , and the pressure  $p = -\omega$  are the same for both states. These quantities do not change in value as one takes the system across the coexistence region by increasing the average density in the system (or equivalently  $\phi_0$ ). This is because the additional surface excess free-energy terms (surface tension terms that are present because both coexisting phases are in the system) do not contribute in the thermodynamic limit. This is in turn a consequence of the fact that these surface terms scale as  $L^{(d-1)}$ , whereas the bulk volume terms scale as  $L^d$ , where  $d$  is the dimensionality of the system. Thus, regions where these measures are approximately flat are in a coexistence region between two phases—this can be confirmed for the 2D results by comparing the ranges of  $\phi_0$ , where the results for  $\mu$  and  $\omega$  are approximately flat, with the coexistence regions in Fig. 10. The observation that the 2D curves in Fig. 13 are not completely flat indicates that the interfacial (surface tension) terms between the different phases in the LS state do contribute to the free energy, and thus is a finite-size effect. Note that it might be possible to distribute the LS in such a way that they percolate throughout the whole system so that the contribution

from the interfaces scales as  $L^d$ . If this is the case, the above argument does not apply.

## V. DISCUSSION AND CONCLUSIONS

The conserved Swift-Hohenberg equation is perhaps the simplest example of a pattern-forming system with a conserved quantity. Models of this type arise when modeling a number of different systems, with the PFC model being one particular example. Other examples include binary fluid convection between thermally insulating boundaries [26] (where this equation was first derived), convection in an imposed magnetic field (where the conserved quantity is the magnetic flux [20,21]), and two-dimensional convection in a rotating layer with stress-free boundaries (where the conserved quantity is the zonal velocity [20,22]). Models of a vibrating layer of granular material are also of this type (here the conserved quantity is the total mass [50]). It is perhaps remarkable that all these distinct systems behave very similarly. In particular, in one spatial dimension they all share the following features: (i) strongly subcritical bifurcations forming localized structures that may lie outside the bistability region between the homogeneous and periodic states; (ii) the presence of LS even when the periodic branch is supercritical; (iii) organization of LS into slanted snaking; and (iv) the transition from slanted snaking to smooth snaking whereby the LS grow smoothly without specific bump-forming events (referred to as “nucleation” events in the pattern formation literature.<sup>1</sup>) These properties of the system can all be traced to the fact that the conserved quantity is necessarily redistributed when an instability takes place or a localized structure forms. This fact makes it harder for additional LS to form and as a result the system has to be driven harder for this to occur, leading to slanted snaking. Bistability is no longer required since the localized structures are no longer viewed as inclusions of a periodic state within a homogeneous background or vice versa. These considerations also explain why the bifurcation diagrams in these systems are sensitive to the domain size, and it may be instructive, although difficult, to repeat some of our calculations for larger domain sizes. The existence of LS outside the binodal in two and three dimensions remains an open problem.

Of particular significance is the observation that the slanted snaking found when the LS norm  $\|\delta\phi\|$  is plotted as a function of the mean order parameter  $\phi_0$  for fixed  $r$  (Figs. 2 and 4) is “straightened” out when the same solution branches are displayed as a function of  $\mu$  (see Fig. 14). The snaking is then vertically aligned and centered around the coexistence chemical potential values (referred to as Maxwell points in Ref. [46]) as known from the nonconserved Swift-Hohenberg equation [46]. In this representation, the periodic states typically bifurcate subcritically from the homogeneous state

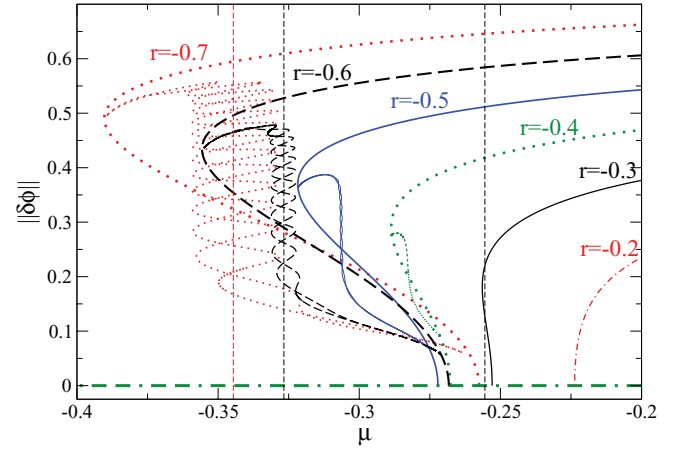


FIG. 14. (Color online) The  $L^2$  norm  $\|\delta\phi\|$  for the homogeneous, periodic, and localized steady-state solutions of the conserved Swift-Hohenberg equation (3) as a function of the chemical potential  $\mu$ , for a fixed domain of size  $L = 100$  and various  $r$ . The horizontal thick dot-dashed green line corresponds to the homogeneous solution  $\phi(x) = \phi_0$ . Periodic solutions with  $n = 16$  peaks are labeled by the corresponding  $r$  values, whereas the branches that bifurcate from them represent the two types of symmetric localized states (LS<sub>odd</sub> and LS<sub>even</sub>):  $r = -0.7$  (dotted red lines),  $r = -0.6$  (dashed black lines),  $r = -0.5$  (solid blue lines),  $r = -0.4$  (dotted green lines),  $r = -0.3$  (solid black line), and  $r = -0.2$  (dot-dashed red line). The dashed vertical lines indicate the corresponding coexistence chemical potential values for  $r = -0.7$ ,  $-0.6$ , and  $-0.3$ , respectively.

(Fig. 14), in contrast to the supercritical transitions found when  $\phi_0$  is used as the bifurcation parameter (Figs. 2 and 4). It is also worth noting that the thermodynamic tricritical point at  $(\phi_{0b}, r_b^{\max}) = (\pm\sqrt{3/38}, -9/38)$  discussed in Sec. II B (see also the last paragraph of the Appendix) corresponds to the transition from a subcritical to a supercritical primary bifurcation in the representation of Fig. 14, i.e., when  $\mu$  is used as the bifurcation parameter. This transition takes place between the solid black line for  $r = -0.3$  and the dashed red line for  $r = -0.2$  in Fig. 14 and implies that the linear stability properties of *identical* periodic solutions differ, depending on whether the permitted perturbations preserve  $\mu$  (and hence permit  $\phi_0$  to vary) or vice versa, and this is so for the localized states as well. In particular, when  $\mu$  is used as the control parameter, the differences identified in Sec. III B between cases (i)–(iv), where the LS branches do not snake, and cases (v) and (vi), where they do snake, disappear. In Fig. 14, snaking over  $\mu$  is clearly visible for  $r = -0.7$ ,  $-0.6$ , and  $-0.5$ . There is no snaking for  $r = -0.4$ , most likely due to finite-size effects.

The thermodynamic reason that the snaking becomes straightened when displayed as a function of the chemical potential  $\mu$  is related to the issues discussed at the end of Sec. IV. For a system with  $(\phi_0, r)$  chosen so that it is in the coexistence region (e.g., between the homogeneous and the bump states) and size  $L$  large enough to be considered to be in the thermodynamic limit  $L \rightarrow \infty$ , the chemical potential does not vary when  $\phi_0$  is changed and neither does the grand potential  $\omega = -p$ . This is because the free-energy contribution from interfaces between the coexisting phases (the interfacial tension) scales with the system size as  $L^{d-1}$ , and hence is

<sup>1</sup>In the condensed-matter literature, the word “nucleation” refers to the traversing of a (free) energy barrier to form a new phase. In the theory of pattern formation, this term is used more loosely to describe the appearance or birth of a new structure, bump, etc., without necessarily implying that there is an energy barrier to be crossed.

negligible compared to the bulk contributions which scale as  $L^d$ . As  $\phi_0$  is varied so as to traverse the coexistence region, new bumps are added or removed from the bump state (LS). For a (thermodynamically) large system, the resulting changes in the free energy are negligible, although this is no longer true of a finite-size system. Furthermore, the interfacial free-energy contribution between the two phases varies depending on the size of the bumps right at the interface, and the size of these bumps depends on the value of  $\phi_0$ . The difference between the maximal interfacial energy and the minimal value determines the width of the snake. All of these contributions have leading-order terms that scale as  $L^{-1}$ . In a related situation, the variation in the chemical potential as the density is varied in a finite-size system containing a fluid exhibiting gas-liquid coexistence is discussed in Refs. [59–61]. It is instructive to compare, for example, Fig. 3 in Ref. [61] and Fig. 13(c) of the present paper.

We mention that the steady states of the nonconserved Swift-Hohenberg equation studied, e.g., in Refs. [46,49], correspond to solutions of Eq. (5) with the nonlinearity  $g_{23}$  but  $\mu = 0$  (see Sec. II A). These always show vertically aligned snaking when the LS norm  $\|\delta\phi\|$  is plotted as a function of  $r$  (adapting  $\phi_0$ ). However, when  $\mu = 0$  no localized states are present with the pure cubic nonlinearity employed in Eq. (5). To find such states,  $\mu$  must be fixed at a value sufficiently far from zero; the resulting LS then exhibit vertically aligned snaking when plotted as a function of  $r$  [46].

The domain size we have used,  $L = 100$ , is moderately large. It contains of the order of 16 wavelengths of the primary structure-forming instability. Because the equation is simpler than the hydrodynamic equations for which similar behavior was observed, the results we have been able to obtain are substantially more complete, even in one dimension, than was possible elsewhere. In particular, we have been able to compute the rungs of asymmetric LS and to study their behavior as the system transitions from slanted snaking to smooth snaking as  $r$  increases toward zero. The extension of our results to two and three spatial dimensions is necessarily incomplete, although the transition to clusters of bumps followed by isolated bumps as the total “mass” decreases is not surprising. However, the transition from a connected structure to a disconnected one (the “percolation” threshold) in two and three dimensions deserves a much more detailed study than we have been able to provide.

In this connection, we mention two experimental systems exhibiting a transition from a solidlike phase to a gaslike phase of individual spots. This is the gaseous discharge system studied by Purwins and colleagues [17,62] and the liquid-crystal light valve experiment of Residori and colleagues [2]. In both these systems, a crystal-like structure of spots with hexagonal coordination was observed to melt into a “gas” of individual spots as a parameter was varied. This two-dimensional process leads to states resembling those found here in Figs. 10 and 11, although the stripe-like structures were typically absent. In these two systems, the spots in the “gas-phase” are mobile unlike in the cSH equation, indicating the absence of variational structure. However, both systems are globally coupled by the imposed potential difference in the discharge system and the feedback loop in the liquid crystal light valve experiment, raising the possibility that the global

coupling in these systems plays a similar role to the role played by the conserved order parameter in the cSH equation.

We should also mention that some of the localized states observed in Figs. 11 and 12 raise some concern about the validity of the PFC as a model for solidification and freezing—we refer in particular to the order-parameter profiles displayed at the bottom right of these figures. These show that in both two and three dimensions the PFC predicts the existence of steady states with isolated single bumps. Recall that in the standard interpretation of the PFC, the bumps correspond to frozen particles while the homogeneous state corresponds to the uniform liquid state. Such profiles could perhaps be a signature of the dynamical heterogeneity that is a feature of glassy systems, but there are problems with this interpretation. The glass transition is a collective phenomenon—single particles do not freeze on their own while the remainder of the particles around them remain fluid. We refer readers interested in the issue of the precise interpretation of the order parameter in the PFC to the discussion in the final section of Ref. [63]. We should also point out that although these structures correspond to local minima of the free energy (i.e., they are stable), they do not correspond to the global minimum. These states occur for state points where the global free-energy minimum corresponds to the uniform homogeneous state.

All the results presented here have been obtained for the generic conserved Swift-Hohenberg equation, Eq. (1), with the energy functional in Eq. (2). We believe that our main results provide a qualitative description of a number of related models in material science that are of a similar structure and describe systems that may show transitions between homogeneous and patterned states characterized by a finite structure length. In particular, we refer to systems that can be described by conserved gradient dynamics based on an underlying energy functional that features a local double-well contribution, a destabilizing squared gradient term, and a stabilizing squared Laplacian term. The latter two terms may themselves result from a gradient expansion of an integral describing nonlocal interactions such as that required to reduce DDFT models to the simpler PFC model [27,28].

Other systems, where the present results may shed some light, include diblock copolymers and epitaxial layers. The time evolution equation for diblock copolymers [64–68] is of fourth order, as is the nonconserved SH equation, but contains a global coupling term that is related to mass conservation. The equation emerges from a nonlocal term in the energy functional [69,70]. The global coupling results in an evolution toward a state with a given mean value for the density order parameter  $\phi_0$  if the initial value is different from  $\phi_0$  or in a conservation of mass as the system evolves if the initial value coincides with the imposed  $\phi_0$ . Although this differs from the formulation using a conserved Swift-Hohenberg equation, the steady versions of the diblock-copolymer equation and of the conserved Swift-Hohenberg equation are rather similar: they only differ in the position of the nonlinearity. Up to now, no systematic study of localized states exists for the diblock-copolymer equation, although Ref. [68] discusses their existence and gives some numerical examples for a profile with a single bump in rather small systems (see their Fig. 5). Since in the diblock-copolymer system the order parameter is a conserved quantity, we would expect the snaking of localized

states for fixed  $\phi_0$  to be slanted similar to our Fig. 2, instead of being vertical, corresponding to a standard snake, where all the saddle-node bifurcations are vertically aligned, as sketched in Fig. 6 of Ref. [68].

Finally, we briefly mention a group of model equations that are derived to describe the evolution of the surface profile of epitaxially strained solid films including, e.g., the self-organization of quantum dots [71]. The various evolution equations that have been employed account for the elasticity (linear and nonlinear isotropic elasticity, as well as misfit strain) of the epitaxial layer and the (isotropic or anisotropic) wetting interaction between the surface layer and the solid beneath. The evolution equations we wish to highlight are of sixth order [72–75] much like the conserved Swift-Hohenberg equation investigated here. Other models, however, are of fourth order only [76,77] or contain fully nonlocal terms (resulting in integro-differential equations) [78,79]. However, even the sixth-order models often contain additional nonlinear terms in the derivatives (see, for instance, Eq. (5) of Ref. [71]). Localized solutions of these equations have to our knowledge not yet been studied systematically, although some have been obtained numerically (see Fig. 5 of Ref. [71]). Future research should investigate how the characteristics of the localized states analyzed here for the conserved Swift-Hohenberg equation differ from those in specific applied systems such as diblock copolymers or epitaxial layers.

#### ACKNOWLEDGMENTS

The authors wish to thank the EU for financial support under Grant No. MRTN-CT-2004-005728 (MULTIFLOW) and the National Science Foundation for support under Grant No. DMS-1211953.

#### APPENDIX

In this Appendix, we determine the direction of branching of the localized states when they bifurcate from the branch of periodic states. When the domain is large, this bifurcation occurs when the amplitude of the periodic states is small and hence is accessible to weakly nonlinear theory.

We begin with Eq. (4), which may be written

$$\phi_t = \alpha \partial_x^2 [(r + q^4)\phi + \phi^3 + 2q^2 \partial_x^2 \phi + \partial_x^4 \phi]. \quad (\text{A1})$$

This equation has the homogeneous solution  $\phi = \phi_0$ . We let  $\phi = \phi_0 + \psi$ , obtaining

$$\begin{aligned} \psi_t = \alpha \partial_x^2 [(r + q^4 + 3\phi_0^2)\psi + 3\phi_0 \psi^2 + \psi^3 \\ + 2q^2 \partial_x^2 \psi + \partial_x^4 \psi]. \end{aligned} \quad (\text{A2})$$

Linearizing and looking for solutions of the form  $\psi \propto \exp(\beta t + ikx)$ , we obtain the dispersion relation

$$\beta = -\alpha k^2 [r + (q^2 - k^2)^2 + 3\phi_0^2]. \quad (\text{A3})$$

The condition  $\beta = 0$  gives the critical wave numbers

$$k_c^2 = q^2 \pm \sqrt{-r - 3\phi_0^2}. \quad (\text{A4})$$

Thus when  $r = r_c \equiv -3\phi_0^2$ , the neutral curve has maxima at both  $k = 0$  and  $k_c = q$ . When  $r = -3\phi_0^2 - \epsilon^2 \nu$ , where  $\nu = O(1)$  and  $\epsilon$  is a small parameter that defines how far  $r$  is

from  $r_c$ , a band of wave numbers near  $k = q$  grows slowly with growth rate  $\beta = O(\epsilon^2)$ , while wave numbers near  $k = 0$  decay at the same rate. There is therefore time for these two disparate wave numbers to interact and it is this interaction that determines the direction of branching.

These considerations suggest that we perform a two-scale analysis with a short scale  $x = O(q^{-1})$  and a long scale  $X = \epsilon x$ , so that  $\partial_x \rightarrow \partial_x + \epsilon \partial_X$ , etc. We also write

$$\begin{aligned} \psi = \epsilon A(X, t) e^{iqx} + \epsilon^2 B(X, t) + \epsilon^2 C(X, t) e^{2iqx} \\ + \text{c.c.} + O(\epsilon^3), \end{aligned} \quad (\text{A5})$$

where the amplitudes  $A$  and  $C$  are complex and  $B$  is real. Substituting, we obtain

$$\begin{aligned} A_t = -\epsilon^2 \alpha q^2 (-\nu A - 4q^2 A_{XX} + 6\phi_0 AB + 6\phi_0 CA^* \\ + 3|A|^2 A) + O(\epsilon^3), \end{aligned} \quad (\text{A6})$$

$$B_t = \epsilon^2 \alpha (q^4 B_{XX} + 6\phi_0 |A|_{XX}^2) + O(\epsilon^3), \quad (\text{A7})$$

and

$$C_t = -4\alpha q^2 (9q^4 C + 3\phi_0 A^2) + O(\epsilon). \quad (\text{A8})$$

The last equation implies that the mode  $C$  decays on an  $O(1)$  time scale to its asymptotic value,  $C = -\phi_0 A^2 / 3q^4 + O(\epsilon)$ . The resulting equations may be written in the form

$$\begin{aligned} A_t = \nu A + 4A_{XX} - \xi A \theta_X - 3 \left( 1 - \frac{\xi^2}{54} \right) |A|^2 A + O(\epsilon), \\ \theta_t = \theta_{XX} + \xi |A|_X^2 + O(\epsilon) \end{aligned} \quad (\text{A9})$$

$$\theta_t = \theta_{XX} + \xi |A|_X^2 + O(\epsilon) \quad (\text{A10})$$

using the substitution  $B = \theta_X$ , and integrating Eq. (A7) once to obtain an equation for  $\theta$ . In writing these equations, we have absorbed  $q$  into the length scale  $X$  and  $\epsilon^2 \alpha q^2$  into the time scale  $t$ , and introduced the parameter  $\xi \equiv 6\phi_0 / q^2 < 0$ . The resulting equations are equivalent to the equations studied by Matthews and Cox [37].

Equations (A9) and (A10) provide a complete description of the small amplitude behavior of Eq. (4). The equations inherit a gradient structure from Eq. (4),

$$A_t = -\frac{\delta F}{\delta A^*}, \quad \theta_t = -\frac{\delta F}{\delta \theta}, \quad (\text{A11})$$

where

$$\begin{aligned} F[A, A^*, \theta] = \int_D \left\{ -\nu |A|^2 + 4|A_X|^2 + \frac{1}{2} \theta_X^2 + \xi |A|^2 \theta_X \right. \\ \left. + \frac{3}{2} \left( 1 - \frac{\xi^2}{54} \right) |A|^4 \right\} dX. \end{aligned} \quad (\text{A12})$$

We may write this energy in the form

$$\begin{aligned} F[A, A^*, \theta] = \int_D \left\{ -\nu |A|^2 + 4|A_X|^2 + \frac{1}{2} \left[ (\theta_X + \xi |A|^2)^2 \right. \right. \\ \left. \left. + 3 \left( 1 - \frac{19\xi^2}{54} \right) |A|^4 \right] \right\} dX, \end{aligned} \quad (\text{A13})$$

implying that the free energy  $F[A, A^*, \theta]$  is not bounded from below once  $\xi^2 > 54/19$  (equivalently  $\phi_0^2 > 3q^4/38$ ). This is a reflection of the presence of subcritical branches. Indeed,



the steady states of Eqs. (A9) and (A10) correspond to critical points of this energy and satisfy the *nonlocal* equation

$$4A_{XX} + (\nu - \langle |A|^2 \rangle)A - 3\left(1 - \frac{19\xi^2}{54}\right)|A|^2A = 0, \quad (\text{A14})$$

where  $\langle (\dots) \rangle \equiv L^{-1} \int_0^L (\dots) dx$  and  $L$  is the domain length. This equation demonstrates (i) that the primary bifurcation is subcritical when  $\xi^2 > 54/19$  in agreement with Eq. (A13), and (ii) that as  $|A|$  increases the value of  $\nu$  has to be raised in order to maintain the same value of the effective bifurcation parameter  $\nu_{\text{eff}} \equiv \nu - \langle |A|^2 \rangle$ . This is the basic reason behind the slanted structure in Fig. 2(a). Equations of this type arise in numerous applications [22,80–82] and their properties have been studied in several papers [81,83–85]. We mention, in particular, that unmodulated wave trains bifurcate supercritically when  $\xi^2 < 54$ , a condition that differs from the corresponding condition  $\xi^2 < 54/19$  for spatially modulated wave trains.

Equations (A9) and (A10) possess the solution  $(A, \theta) = (A_0, 0)$ , where  $|A_0|^2 = \nu/[3(1 - \xi^2/54)]$ , corresponding to a spatially uniform wave train. This state bifurcates in the positive  $\nu$  direction wherever  $\xi^2 < 54$ , or equivalently  $\phi_0^2 < 3q^4/2$ . In the following we are interested in the modulational instability of this state. We suppose that this instability takes place at  $\nu = \nu_c$  and write  $\nu = \nu_c + \delta^2\tilde{\nu}$ , where  $\delta \ll \epsilon$  is a new small parameter and  $\tilde{\nu} = O(1)$ . In addition, we write  $A = A_0(1 + \tilde{A})$ ,  $\theta_X = \tilde{V}$ . Since the imaginary part of  $\tilde{A}$  decays to zero, we take  $\tilde{A}$  to be real and write

$$\begin{aligned} \tilde{A} &= \delta\tilde{A}_1 + \delta^2\tilde{A}_2 + \delta^3\tilde{A}_3 + \dots, \\ \tilde{V} &= \delta\tilde{V}_1 + \delta^2\tilde{V}_2 + \delta^3\tilde{V}_3 + \dots. \end{aligned} \quad (\text{A15})$$

Finally, since the localized states created at  $\nu_c$  are stationary, we set the time derivatives to zero and integrate Eq. (A10) once obtaining

$$\tilde{V} + \xi|A|^2 + C(\delta) = 0, \quad (\text{A16})$$

where  $C = C_0 + \delta C_1 + \delta^2 C_2 + \delta^3 C_3 + \dots$  and the  $C_j$  are determined by the requirement that the average of  $V$  over the domain vanishes.

Substitution of the above expressions yields a sequence of ordinary differential equations which we solve subject to periodic boundary conditions. At  $O(1)$  we obtain  $C_0 = -\xi|A_c|^2$ , where  $A_c$  denotes the value of  $A_0$  at  $\nu = \nu_c$ . At  $O(\delta)$  we obtain the linear problem

$$\begin{aligned} -2\nu_c\tilde{A}_1 + 4\tilde{A}_{1XX} - \xi\tilde{V}_1 &= 0, \\ \tilde{V}_1 + 2\xi|A_c|^2\tilde{A}_1 &= 0, \quad C_1 = 0, \end{aligned} \quad (\text{A17})$$

and conclude that  $\tilde{A}_1 = A_{11} \cos \ell X$ ,  $\tilde{V}_1 = V_{11} \cos \ell X$ , provided that  $\nu_c = -2\ell^2[(1 - \xi^2/54)/(1 - 19\xi^2/54)]$ . Note that this quantity is positive when  $54 > \xi^2 > 54/19$  (equivalently  $3q^4/2 > \phi_0^2 > 3q^4/38$ ) and that it vanishes in the limit  $\ell \rightarrow 0$ , i.e., for infinite modulation length scale.

At  $O(\delta^2)$  we obtain

$$\begin{aligned} -2\nu_c\tilde{A}_2 + 4\tilde{A}_{2XX} - \xi\tilde{V}_2 &= \xi\tilde{A}_1\tilde{V}_1 + 3\nu_c\tilde{A}_1^2, \\ \tilde{V}_2 + \xi|A_c|^2(2\tilde{A}_2 + \tilde{A}_1^2) + C_2 &= 0. \end{aligned} \quad (\text{A18})$$

Thus  $\tilde{A}_2 = A_{20} + A_{22} \cos 2\ell X$ ,  $\tilde{V}_2 = V_{20} + V_{22} \cos 2\ell X$ , where

$$\begin{aligned} A_{20} &= -\frac{3}{4} \left[ \frac{1 - (13\xi^2/54)}{1 - (\xi^2/54)} \right] A_{11}^2, \quad A_{22} = \frac{1}{4} A_{11}^2, \\ V_{20} &= -\xi|A_c|^2 A_{11}^2, \end{aligned} \quad (\text{A19})$$

together with

$$C_2 = -\frac{1}{2}\xi|A_c|^2 A_{11}^2 - 2\xi|A_c|^2 A_{20}. \quad (\text{A20})$$

Finally, at  $O(\delta^3)$  we obtain

$$\begin{aligned} -2\nu_c\tilde{A}_3 + 4\tilde{A}_{3XX} - \xi\tilde{V}_3 \\ = 2\tilde{\nu}\tilde{A}_1 + \xi(\tilde{A}_1\tilde{V}_2 + \tilde{A}_2\tilde{V}_1) + \nu_c(6\tilde{A}_1\tilde{A}_2 + \tilde{A}_1^3) \end{aligned} \quad (\text{A21})$$

and

$$\tilde{V}_3 + \xi|A_c|^2(2\tilde{A}_3 + 2\tilde{A}_1\tilde{A}_2) + C_3 = -\frac{2\xi}{3[1 - (\xi^2/54)]}\tilde{\nu}\tilde{A}_1. \quad (\text{A22})$$

The direction of branching of solutions with  $\tilde{A} \neq 0$  follows from the solvability condition for  $\tilde{A}_3$ , i.e., the requirement that the inhomogeneous terms contain no terms proportional to  $\cos \ell X$ . We obtain

$$\tilde{\nu} + 3\ell^2\tilde{A}_{11}^2 \left[ \frac{1 - (13\xi^2/54)}{1 - (19\xi^2/54)} \right] = 0. \quad (\text{A23})$$

It follows that the localized states bifurcate in the positive  $\nu$  direction (lower temperature) when  $54/19 < \xi^2 < 54/13$  and in the negative  $\nu$  direction when  $54/13 < \xi^2 < 54$ . The former requirement is equivalent to  $3q^4/38 < \phi_0^2 < 3q^4/26$ , the latter to  $3q^4/26 < \phi_0^2 < 3q^4/2$ . These results agree with the corresponding results for an equation similar to Eq. (A14) obtained by Elmer [81] (see also [22,37]).

In the above calculation, we have fixed the parameter  $\xi$  (equivalently  $\phi_0$ ) and treated  $r$  (equivalently  $\nu$ ) as the bifurcation parameter. However, we can equally well do the opposite. Since the calculation is only valid in the neighborhood of the primary bifurcation at  $r = -3\phi_0^2$ , i.e., in the neighborhood of  $\xi = -\sqrt{-12r}/q^2$ , the destabilizing perturbation analogous to  $\tilde{\nu} > 0$  is now replaced by  $\tilde{\xi} > 0$  (cf. Fig. 1), implying that the direction of branching of localized states changes from subcritical to supercritical as  $\xi^2$  decreases through  $\xi^2 = 54/13$  (equivalently  $\phi_0^2$  decreases through  $\phi_0^2 = 3q^4/26$  or  $r$  increases through  $r = -9q^4/26 \approx -0.35q^4$ ), in good agreement with the numerically obtained value  $r \approx -0.41$  (for  $q = 1$ ) that is indicated in Fig. 7 by the horizontal line separating regions (iii) and (iv).

We next consider the corresponding results in the case when the chemical potential  $\mu$  is fixed. In this case, the constants  $C_j$  vanish, and the  $O(\delta^2)$  problem therefore has solutions of the form  $\tilde{A}_2 = A_{20} + A_{22} \cos 2\ell X$ ,  $\tilde{V}_2 = V_{20} + V_{22} \cos 2\ell X$ , where

$$\begin{aligned} A_{20} &= -\frac{3}{4} A_{11}^2, \quad V_{20} = \xi|A_c|^2 A_{11}^2, \\ A_{22} &= \frac{1}{4} A_{11}^2, \quad V_{22} = -\xi|A_c|^2 A_{11}^2. \end{aligned} \quad (\text{A24})$$

The nonzero  $V_{20}$  contributes additional terms to the solvability condition at  $O(\delta^3)$ . The result corresponding to (A23) is

$$\tilde{\nu} + 3\ell^2\tilde{A}_{11}^2 \left[ \frac{1 - (\xi^2/54)}{1 - (19\xi^2/54)} \right] = 0. \quad (\text{A25})$$

This implies that the secondary LS branches are subcritical whenever the periodic branch is supercritical ( $\xi^2 < 54$ ) and the secondary bifurcation is present ( $\xi^2 > 54/19$ ). These results are consistent with Fig. 14 and moreover predict

that the LS states are absent for  $\xi^2 < 54/19$ , i.e., for  $\phi_0 > -\sqrt{3/38}q^2$  or  $r > -9q^4/38$  (cf. Fig. 14). This point is, of course, the thermodynamic tricritical point discussed in Sec. II B.

- 
- [1] P. Coulet, C. Riera, and C. Tresser, *Phys. Rev. Lett.* **84**, 3069 (2000).
- [2] U. Bortolozzo, M. G. Clerc, and S. Residori, *New J. Phys.* **11**, 093037 (2009).
- [3] R. Richter and I. V. Barashenkov, *Phys. Rev. Lett.* **94**, 184503 (2005).
- [4] G. W. Hunt, M. A. Peletier, A. R. Champneys, P. D. Woods, M. A. Wadee, C. J. Budd, and G. J. Lord, *Nonlin. Dyn.* **21**, 3 (2000).
- [5] O. Batiste, E. Knobloch, A. Alonso, and I. Mercader, *J. Fluid Mech.* **560**, 149 (2006).
- [6] A. Bergeon and E. Knobloch, *Phys. Fluids* **20**, 034102 (2008).
- [7] S. Blanchflower, *Phys. Lett. A* **261**, 74 (1999).
- [8] T. M. Schneider, J. F. Gibson, and J. Burke, *Phys. Rev. Lett.* **104**, 104501 (2010).
- [9] O. Lioubashevski, H. Arbell, and J. Fineberg, *Phys. Rev. Lett.* **76**, 3959 (1996).
- [10] J. Rajchenbach, A. Leroux, and D. Clamond, *Phys. Rev. Lett.* **107**, 024502 (2011).
- [11] P. B. Umbanhowar, F. Melo, and H. L. Swinney, *Nature (London)* **382**, 793 (1996).
- [12] T. Ackemann, W. J. Firth, and G.-L. Oppo, in *Fundamentals and Applications of Spatial Dissipative Solitons in Photonic Devices*, in *Advances in Atomic, Molecular and Optical Physics*, Vol. 57, edited by P. R. Berman, E. Arimondo, and C.-C. Lin (Elsevier, Amsterdam, 2009), pp. 323–421.
- [13] P. Kolodner, D. Bensimon, and C. M. Surko, *Phys. Rev. Lett.* **60**, 1723 (1988).
- [14] W. Barten, M. Lücke, and M. Kamps, *Phys. Rev. Lett.* **66**, 2621 (1991).
- [15] M. Dennin, G. Ahlers, and D. S. Cannell, *Science* **272**, 388 (1996).
- [16] H. Riecke and G. D. Granzow, *Phys. Rev. Lett.* **81**, 333 (1998).
- [17] H.-G. Purwins, H. U. Boedeker, and S. Amiranashvili, *Adv. Phys.* **59**, 485 (2010).
- [18] Y. Pomeau, *Physica D* **23**, 3 (1986).
- [19] J. Burke and E. Knobloch, *Chaos* **17**, 037102 (2007).
- [20] S. M. Cox and P. C. Matthews, *Physica D* **149**, 210 (2001).
- [21] D. Lo Jacono, A. Bergeon, and E. Knobloch, *J. Fluid Mech.* **687**, 595 (2011).
- [22] C. Beaume, A. Bergeon, H.-C. Kao, and E. Knobloch, *J. Fluid Mech.* **717**, 417 (2013).
- [23] W. J. Firth, L. Columbo, and A. J. Scroggie, *Phys. Rev. Lett.* **99**, 104503 (2007).
- [24] J. H. P. Dawes, *SIAM J. Appl. Dyn. Syst.* **7**, 186 (2008).
- [25] H. Emmerich, H. Löwen, R. Wittkowski, T. Gruhn, G. Tóth, G. Tegze, and L. Gránásy, *Adv. Phys.* **61**, 665 (2012).
- [26] E. Knobloch, *Phys. Rev. A* **40**, 1549 (1989).
- [27] S. van Teeffelen, R. Backofen, A. Voigt, and H. Löwen, *Phys. Rev. E* **79**, 051404 (2009).
- [28] A. J. Archer, M. J. Robbins, U. Thiele, and E. Knobloch, *Phys. Rev. E* **46**, 031603 (2012).
- [29] G. Tegze, L. Granasy, G. I. Toth, F. Podmaniczky, A. Jaatinen, T. Ala-Nissila, and T. Pusztai, *Phys. Rev. Lett.* **103**, 035702 (2009).
- [30] G. Tegze, G. Bansel, G. I. Toth, T. Pusztai, Z. Y. Fan, and L. Granasy, *J. Comput. Phys.* **228**, 1612 (2009).
- [31] G. Tegze, L. Granasy, G. I. Toth, J. F. Douglas, and T. Pusztai, *Soft Matter* **7**, 1789 (2011).
- [32] T. Pusztai, G. Tegze, G. I. Toth, L. Kornyei, G. Bansel, Z. Y. Fan, and L. Granasy, *J. Phys.: Condens. Matter* **20**, 404205 (2008).
- [33] D. J. B. Lloyd, B. Sandstede, D. Avitabile, and A. R. Champneys, *SIAM J. Appl. Dyn. Syst.* **7**, 1049 (2008).
- [34] D. Avitabile, D. J. B. Lloyd, J. Burke, E. Knobloch, and B. Sandstede, *SIAM J. Appl. Dyn. Syst.* **9**, 704 (2010).
- [35] D. J. B. Lloyd and B. Sandstede, *Nonlinearity* **22**, 485 (2009).
- [36] S. G. McCalla and B. Sandstede, *Physica D* **239**, 1581 (2010).
- [37] P. C. Matthews and S. M. Cox, *Nonlinearity* **13**, 1293 (2000).
- [38] S. M. Cox, *Phys. Lett. A* **333**, 91 (2004).
- [39] K. R. Elder, M. Katakowski, M. Haataja, and M. Grant, *Phys. Rev. Lett.* **88**, 245701 (2002).
- [40] C. V. Achim, J. A. P. Ramos, M. Karttunen, K. R. Elder, E. Granato, T. Ala-Nissila, and S. C. Ying, *Phys. Rev. E* **79**, 011606 (2009).
- [41] P. Galenko, D. Danilov, and V. Lebedev, *Phys. Rev. E* **79**, 051110 (2009).
- [42] P. Stefanovic, M. Haataja, and N. Provatas, *Phys. Rev. Lett.* **96**, 225504 (2006).
- [43] R. Backofen, A. Ratz, and A. Voigt, *Philos. Mag. Lett.* **87**, 813 (2007).
- [44] H. Ohnogi and Y. Shiwa, *Physica D* **237**, 3046 (2008).
- [45] J. Mellenthin, A. Karma, and M. Plapp, *Phys. Rev. B* **78**, 184110 (2008).
- [46] J. Burke and E. Knobloch, *Phys. Rev. E* **73**, 056211 (2006).
- [47] E. Doedel, H. B. Keller, and J. P. Kernevez, *Int. J. Bifurcation Chaos* **1**, 493 (1991).
- [48] E. J. Doedel and B. E. Oldeman, *AUTO07p: Continuation and Bifurcation Software for Ordinary Differential Equations* (Concordia University, Montreal, 2009).
- [49] A. Bergeon, J. Burke, E. Knobloch, and I. Mercader, *Phys. Rev. E* **78**, 046201 (2008).
- [50] J. H. P. Dawes and S. Lilley, *SIAM J. Appl. Dyn. Syst.* **9**, 238 (2010).
- [51] J. Burke and E. Knobloch, *Multipulse States in the Swift-Hohenberg Equation*, *Discrete and Continuous Dynamical Systems Suppl.* 109–117 (2009).
- [52] J. Knobloch, D. J. B. Lloyd, B. Sandstede, and T. Wagenknecht, *J. Dyn. Diff. Eq.* **23**, 93 (2011).
- [53] M. Beck, J. Knobloch, D. J. B. Lloyd, B. Sandstede, and T. Wagenknecht, *SIAM J. Math. Anal.* **41**, 936 (2009).
- [54] J. Burke, S. M. Houghton, and E. Knobloch, *Phys. Rev. E* **80**, 036202 (2009).

- [55] H. Gomez and X. Nogueira, *Comput. Meth. Appl. Mech. Eng.* **249–252**, 52 (2012).
- [56] T. Hughes, J. Cottrell, and Y. Bazilevs, *Comput. Meth. Appl. Mech. Eng.* **194**, 4135 (2005).
- [57] H. Gomez, V. Calo, Y. Bazilevs, and T. Hughes, *Comput. Meth. Appl. Mech. Eng.* **197**, 4333 (2008).
- [58] T. K. Callahan and E. Knobloch, *Nonlinearity* **10**, 1179 (1997).
- [59] L. G. MacDowell, V. K. Shen, and J. R. Errington, *J. Chem. Phys.* **125**, 034705 (2006).
- [60] M. Schrader, P. Virnau, and K. Binder, *Phys. Rev. E* **79**, 061104 (2009).
- [61] K. Binder, B. J. Block, P. Virnau, and A. Tröster, *Am. J. Phys.* **80**, 1099 (2012).
- [62] Y. A. Astrov and H.-G. Purwins, *Phys. Lett. A* **283**, 349 (2001).
- [63] M. J. Robbins, A. J. Archer, U. Thiele, and E. Knobloch, *Phys. Rev. E* **85**, 061408 (2012).
- [64] Y. Oono and Y. Shiwa, *Mod. Phys. Lett. B* **1**, 49 (1987).
- [65] G. C. Paquette, *Phys. Rev. A* **44**, 6577 (1991).
- [66] T. Teramoto and Y. Nishiura, *J. Phys. Soc. Jpn.* **71**, 1611 (2002).
- [67] K. B. Glasner, *SIAM J. Appl. Math.* **70**, 2045 (2010).
- [68] K. B. Glasner, *Eur. J. Appl. Math.* **23**, 315 (2012).
- [69] L. Leibler, *Macromolecules* **13**, 1602 (1980).
- [70] T. Ohta and K. Kawasaki, *Macromolecules* **19**, 2621 (1986).
- [71] A. Golovin, S. Davis, and P. Voorhees, *Phys. Rev. E* **68**, 056203 (2003).
- [72] B. Spencer, S. Davis, and P. Voorhees, *Phys. Rev. B* **47**, 9760 (1993).
- [73] T. V. Savina, A. A. Golovin, S. H. Davis, A. A. Nepomnyashchy, and P. W. Voorhees, *Phys. Rev. E* **67**, 021606 (2003).
- [74] A. A. Golovin, M. S. Levine, T. V. Savina, and S. H. Davis, *Phys. Rev. B* **70**, 235342 (2004).
- [75] U. Thiele, *J. Phys.: Condens. Matter* **22**, 084019 (2010).
- [76] Y. Xiang and W. E, *J. Appl. Phys.* **91**, 9414 (2002).
- [77] V. Shenoy, A. Ramasubramaniam, and L. Freund, *Surf. Sci.* **529**, 365 (2003).
- [78] Y. Xiang and W. E, *Phys. Rev. B* **69**, 035409 (2004).
- [79] M. Levine, A. Golovin, S. Davis, and P. Voorhees, *Phys. Rev. B* **75**, 205312 (2007).
- [80] P. Hall, *Phys. Rev. A* **29**, 2921 (1984).
- [81] F. J. Elmer, *Physica D* **30**, 321 (1988).
- [82] F. J. Elmer, *J. Phys. Paris, Colloq.* **49**, 1597 (1988).
- [83] J. Norbury, J. Wei, and M. Winter, *Nonlinearity* **15**, 2077 (2002).
- [84] J. M. Vega, *Nonlinearity* **18**, 1425 (2005).
- [85] J. Norbury, J. Wei, and M. Winter, *Euro. J. Appl. Math.* **18**, 129 (2007).